University of Crete

Department of Materials Science and Technology

4D printing of biomaterials scaffolds for Tissue Engineering

Chaniotaki Lefki

Master thesis

Supervisor: Dr. Stratakis Emmanuel

Three-member committee: Dr. Stratakis Emmanuel

Prof. Mitraki Anna

Prof. George Kioseglou

Acknowledgments

At first, I would like to thank Dr.Stratakis Emmanuel who accept me in the Ultrafast Laser Micro and Nano Processing Laboratory, Institute of Electronic Structure and laser (IESL), Foundation for Research and Technology Hellas (FORTH) from my internship until now. For the trust he showed to me in giving me this challenging research project and his patience and guidance, he provided me during this one year. Furthermore, I would like to thank Prof. Mitraki Anna and Prof. Kioseoglou George for accepting to be my supervisor and at my Committee respectively.

Moreover, a big thank to Mr. Andreas Lemonis, Mr. Christos Doulias, Dr. Paraskevi Kavatzikidou and Dr. Eleftheria Babaliari, where they helped me to make this idea a reality and always were by my side for whatever I needed. Mr. A. Lemonis was responsible for all the software programs and he helped Mr. Ch. Doulias in the construction of the set-up Dr. P. Kavatzikidou and Dr. E. Babaliari performed all the experiments with cells. Without their contribution nothing will be possible.

Dr. Manousaki Aleka for her priceless help, collaboration, and patient in the Scanning Electron Microscopy. Dr. Stella Maragaki for helping me in alignment and for taking wettability measurements. At last but not least, all the members of Ultra-fast Laser and Nano-processing team of the Institute of Electronic Structure and Laser for helping me whenever I needed.

Contents

Abstract

The use of Fused Filament Fabrication 3D printer has been launched in the last decade as it is easy to use and accessible to everyone. It is a common way to alter the surface of the 3D printed scaffold after is printed with subtractive manufacturing techniques. The most well-known subtractive techniques used are either with laser (ablation, cutting and others) or with chemical etching. Although, with laser induced ablation or micromachining, you could abstract more specific, small designs up to the diffraction limit and use a variety of materials. Until now, they only alter the surface of the scaffolds and at some of them the second layer by changing of the focus. In this way, you could alter the surface of the scaffold with designs more complex and smaller than the resolution of the FFF 3D printer or you could make it more porous. In this research project, we combined the subtractive and the additive manufacturing technique to construct advanced 4D scaffolds with PLA for tissue engineering applications.

In this work, we changed 2 set-ups before we ended up with the last and better set-up where we combined the Ytterbium Picosecond Fiber Laser, wavelength 1060 nm, a galvo scanner and Fused Filament Fabrication (FFF) 3D printer. The use of Galvo was to scan surfaces 100 times faster and to have less vibrations. Moreover, there are many techniques to make 3D scaffolds, but the FFF is a cheap technique, with resolution approximately 100 µm. With combination of laser and galvo, we managed to make designs that can cover resolution from 1µm to macro scale. So, we could construct ablated structures at any layer of the 3D scaffold and more complex internal designs with laser, with smaller resolution than that of the 3D printer. Also, this combination is material impendent. In addition, there are some biocompatible polymeric filaments (PLA, PCL, PLGA, PEEK, PET, PLLA) but the most well-known and FDA approved is the natural PLA which is the one that we used. PLA is capable for tissue engineering applications because it is biocompatible, biodegradable and it is used in a wide range of applications such as biomedical.

To achieve this novel and advanced 4D printing mix-and-match, we performed many changes at the ender 3 pro printer, we constructed an optical path, and we worked on a new more functional program with python. We could ablate circles, lines and spots only with galvo or we could 3D print designs or we could ablate designs with laser, or we could combine them. Furthermore, we could do many changes in the laser's design such as minimize its dimensions at xy axis, multiply the laser's design, choose the layers that the laser ablation started and stopped and others.

Finally, we managed to make a successful combination of additive manufacturing and subtractive technique to make 4D scaffolds with PLA for tissue engineering applications. We characterized them with SEM (structural and morphological properties), UV-Vis (optical properties after laser treatment) and contact angle measurements. At last, the interaction of these 4D scaffolds with MSC cells was

investigated. Specifically, we studied MSCs proliferation and morphology with SEM. We also observed the effect of the 4D scaffolds in terms of cell cytoskeleton (actin Phalloidin), cell mechanotransduction (YAP/TAZ), cell nucleus (DAPI) and finally osteopontin (OPN) to observe if they will actually differentiate to osteogenic lineage with and without osteogenic differentiation medium at different time points via confocal microscopy

Introduction

Additive manufacturing (AM) or 3D printing is the next generation manufacturing technology that allows manufacturing of complex parts without requiring specialized tooling. Therefore, AM is currently being used in a wide range of applications such as high value consumer products, food, electronics, machinery, aerospace industry, automobiles, medical and dental applications, textile, construction, education, and architecture. AM has various forms that share the same concept of layer-by-layer manufacturing. The most common and the one that we use among all the AM technologies is fused filament fabrication (FFF), also known as fused deposition modeling (FDM). [1]

Furthermore, the biodegradable polymers attracting the increasingly grown interest over the world, we use a natural Poly(lactic acid) filament which is kind of aliphatic polyester derived from naturally occurring lactic acid, has received significant attention. Except for good thermoplasticity and processability, PLA also has good biodegradability and biocompatibility. At last, they use subtractive manufacturing to alter the surface of these scaffolds. The most well-known subtractive techniques used are either with laser (ablation, cutting and others) or with chemical etching. The laser processing is a new and precise way to modify the surface of polymers and it can be used in a variety of materials.[2]

Theoretical part

1.1 Polylactic acid

Poly (lactic acid) (PLA) is derived from renewable and degradable resources such as corn and rice and decomposes through simple hydrolysis into water and carbon dioxide. PLA has received much attention in the last decade not only because of the potential to replace petrochemical plastics, which are associated with environmental pollution and solid waste disposal problems but also because of its relatively high strength, excellent biodegradability, and good biocompatibility. It has many applications such as biomedical, packaging, films that with the heat will shrink, filaments and others.[3]

PLA consists of monomers of lactic acid. Lactic acid (2-hydroxypropionic acid) is a simple chiral molecule that exists as two enantiomers, L- and D-lactic acid (Fig. 1), which differ in their effect on polarized light.[3]

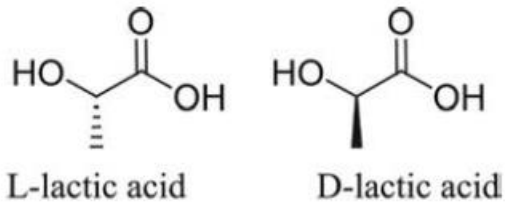

Figure 1: Optical isomers of polylactic acid.[3]

Moreover, the majority of fermentation processes produce predominantly the L-isomer. Therefore, the lactic acid is predominantly L-type. But the L-lactic acid can racemize under certain reaction conditions and convert to another isomer, the D-lactic acid. The presence of equal amount of L- and D-type of lactic acid leads to meso-lactic acid. PLA that purely composed of L- lactic acid or D-lactic acid is called PLLA or PDLA respectively, while PLA that composed of meso-lactic acid is called PDLLA or meso-PLA. The commercial PLA is a copolymer of PLLA and PDLLA. The arrangement of L- and D-lactic acid or the stereochemical structure determines almost all the properties of PLA. The ability to control the stereochemical architecture allows precise control over the speed and degree of crystallinity, the mechanical properties, and the processing temperature of the material.[3]

1.2 Synthesis

PLA can be prepared by different polymerization process from lactic acid including: polycondensation, ring opening polymerization and by direct methods like azeotropic dehydration and enzymatic polymerization. Currently, direct polymerization and ring opening polymerization are the most used production techniques. Figure 2 shows the main methods for PLA synthesis.[4]

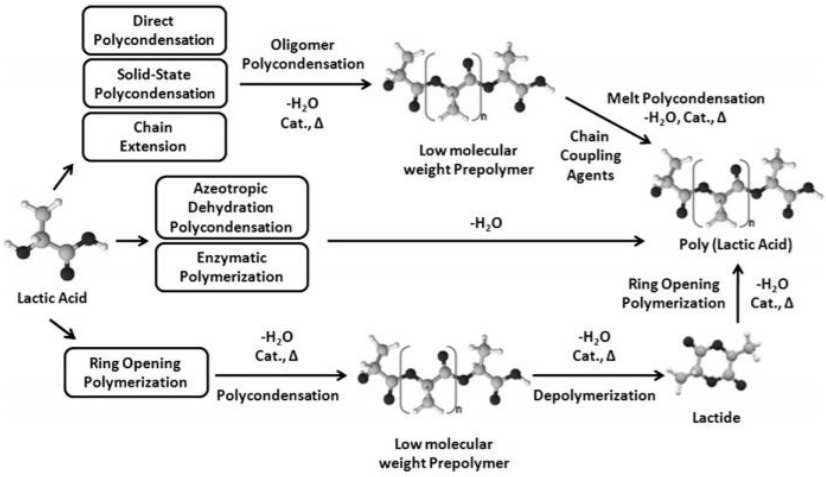

Figure 2: Composition of Polylactic acid[4]

Ring-opening polymerization (ROP) is the most commonly route to achieve high molecular weight. This process occurs by ring opening of the lactic acid cyclic dimmer (lactide) in the presence of catalyst. The process consists of three steps:

polycondensation, depolymerization and ring opening polymerization (see Figure 2). This route requires additional steps of purification which is relatively complicated and expensive. Catalytic ring-opening polymerization of the lactide intermediate results in PLA with controlled molecular weight. By controlling residence time and temperatures in combination with catalyst type and concentration, it is possible to control the ratio and sequence of D- and L-lactic acid units in the final polymer.[4]

1.3 Properties of PLA

In our case, we use the FDA approved natural PLA filament which consists from 100% pure PLA in order to use it as a scaffold. Some important properties of PLA are presented in the tables below.

Table 1: General abilities of PLA filament[25]	
Temperature of Bed (°C)	20-60
Temperature of Head (°C)	180-220
Smokes	Few
Biodegradable/Biocompatible	Yes
Soluble in water	Yes

Table 2: Mechanical abilities of PLA[25]	
Elasticity (GPa)	3.5
Shear meter (GPa)	2.4
Tensile strength (MPa)	50

Table 2: Thermal properties of PLA[25]	
Thermal conductivity (W/m-K)	0.69
Heat capacity (J/Kg-K))	1800
Thermal expansion (um/m-k)	41
Thermal diffusion (mm^2/sec)	0.072
Melting point (Celsius)	180-220
Glass transition (Celsius)	60-65

2.1 Additive manufacturing

The concept of additive manufacturing (AM) that is most referred to as rapid prototyping (RP) and free-form fabrication is governed by 3D printing (3DP), which covers a set of techniques that use a layer-by-layer which involves using a computer-based 3D model, a 3D printer, and a step after the printing activity to fabricate a physical model based on the initial model design. They usually are with a small size, in low quantities, and with a complex, tailored design. Such characteristics have been identified to be vastly beneficial in the biomedical industry amongst others, including the healthcare, aerospace, construction, automotive, food and dental industries. 3DP requires no mold tool and offers near-net-shape manufacturing in a relatively short period of time: a feature that is most beneficial in customized part and product production while being capable of harnessing digital information for the realization of a robust, decentralized 3D manufacturing system.[5]

There are many different AM techniques, they will be described in brief below:

1. **Material Extrusion (ME):** heats the material and selectively dispensed through a nozzle to form a 3D part. In this category are included the Direct Ink Writing (DIW), Fused Modeling Deposition (FMD) and Fused Filament Fabrication (FFF) which is the technique that we use and will be described below. [5]
2. **Material Jetting (MJ):** It is similar technique with stereolithography, involves the selective deposition of a photopolymer and initiator as build material (in the form of droplets) to form thin layers that are further cured to form the 3D part. These systems use machines with an inkjet head and include the popular polyjet machine.[5]
3. **Binder Jetting (BJ):** is based on bonding powder materials with the aid of a liquid bonding agent; to form the 3D part. The liquid bonding agent is selectively deposited to enable a selective fusion process.[5]
4. **Sheet lamination (SL):** involves bonding sheets or foils of material together to form an object.
5. **Vat photo Polymerization (VP):** liquid photopolymer is placed inside a moveable vat, and selectively cured using an ultraviolet light-activated polymerization process. Numerous lithography-based AM approaches like digital light stereolithography (SLA) as well as processing (DLP) can be classified and included in this AM category.[5]
6. **Powder Bed Fusion (PBF):** it uses thermal energy to fuse regions of the powder bed of the build material. Selective laser sintering (SLS), electron beam melting (EBM), and selective laser melting (SLM) fall into this category of AM processes.[5]
7. **Directed Energy Deposition (DED):** this technique has a focused beam of thermal energy (e.g. in laser or plasma arc technologies) to fuse metal and metal-hybrid materials by controlled melting while being deposited. Laser deposition (LD), laser-engineered net shaping (LENS), and plasma arc melting are some of the main technologies within this category.[5]

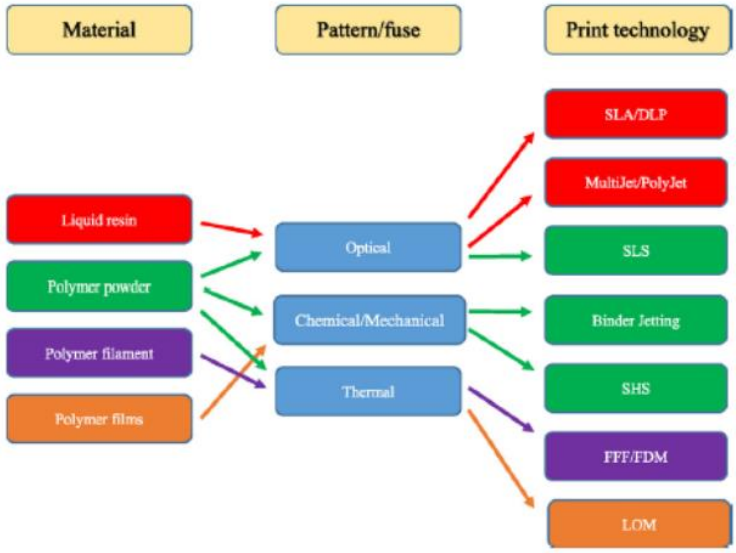

Figure 3: The different Additive manufacturing techniques[6]

8. **Bioprinting:** Bioprinting is another 3D fabrication technique which prints complex tissue constructs using hydrogels that are loaded with cells to print. Bioprinting has three major process approaches: inkjet, extrusion, and laser-assisted bioprinting which are described below. *Inject Bioprinting*: Thermal and piezoelectric inkjet bioprinters are more frequently used for tissue engineering applications. In thermal inkjet bioprinting, a prepolymer solution which can contain cells, known as the bioink, is loaded in an ink cartridge. The cartridge is placed in the printer head which is controlled by a computer and small droplets of ink are ejected by the help of small air bubbles created by heat in the printing head. The working principle of the piezoelectric inkjet bioprinter is based on applying different potentials to the piezoelectric crystal in the bioprinter, and this generates the pressure needed to eject the bioink droplets from the nozzle. The major advantages of inkjet bioprinting are its fast fabrication and the affordability of the device. *Extrusion Bioprinting:* an advanced version of inkjet bioprinting, dispenses bioink using pneumatic (air pressure) or mechanical (screw or piston) systems. In the pneumatic system, bioink is extruded from the nozzle or needle as an uninterrupted cylindrical filament by applying continuous air pressure instead of single droplets. This provides high structural integrity to the product (Knowlton et al., 2018). The mechanical system enables a more direct control over the flow of bioink because of the screw extruding the material. Although, at the both of them, the nozzle may clog due to cell aggregation, high viscosity of the ink or drying of the inject material into the nozzle. *Laser-Assisted Bioprinting (LAB):* consists of a pulsed laser source, a donor layer, and a receiving substrate. The principle of LAB is that bioink is placed below a ribbon which also contains a thin, energy absorbing layer. It has advantages, including not clogging due to the absence of a nozzle and not causing any mechanical stress on the cells because of its noncontact printing approach. All of these increase the cell viability. Although, the LAB system is more expensive compared to other bioprinters.[7]

2.1.1 Fused filament fabrication

Fused filament fabrication (FFF) (or fused deposition modeling – FDM) was developed in the early 1990s as another 3Dprinting approach that like SLS uses preformed polymer as the building material. Fused Deposition Modelling (FDM) is a widely propagated method of additive manufacturing technology, in which thermoplastic polymer in shape of wire (called filament) is melted and extruded through the nozzle with fine diameter. Processed material, in semi-liquid state, is added layer-by-layer. Each cross section is formed due to print-head movement (in X and Y axis). [6] In order to print the desire design, you have to design it on three-dimensional computer aided design (3D CAD) mode. Then, you have to convert it to stereolithography file in order for the slicer program (Cura) to understand it and to change the parameters of the design, slice it into layers and convert it into G-Code file. FDM has many advantages, such as good efficiency, easy material replacement, patient specific designs and its low costs of operation and implementation. Furthermore, building process is automated and does not require the use of any tooling. FDM has also several limitations such as narrow selection of possible to process biomedical materials and resolution up to a few tens of microns. Mechanical properties of thermoplastics processed using FDM in comparison to traditional manufacturing technologies are characterized by lower parameters, which results in a shorter lifetime of such products.[8]

Materials mainly used in Fused Deposition Modelling are acrylonitrile butadiene styrene (ABS), polylactic acid (PLA), polycaprolactone (PCL), polyethylene terephthalate glycol (PET-G), tricalcium phosphate (TCP), nylon. Unfortunately, there is a problem with incorporation of cells or bioactive molecules into filament at the stage of the production or this is usually inefficient process. For biological applications, thermoplastic materials such as PCL, poly(lactic acid) (PLA), and PLGA, often also combined with biomaterials, have been used with FDM to create tissue-engineered scaffolds with low melting temperature. [9]

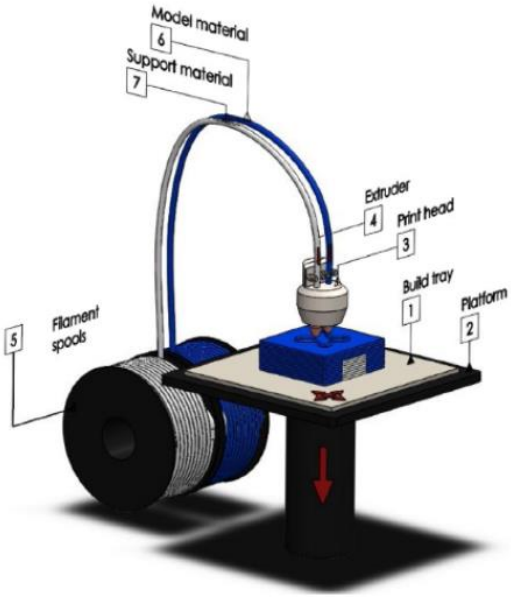

Figure 4: The structure of FFF technique. [8]

2.2 Settings of slicing program (CURA)

The slicing program has the potential to adjust the parameters of the design for example the kind of the support, the layer height and the view options.

The parameters of the design, like the layer height, the thickness of the wall, the infill, the printing temperature, the printing speed, and many others. The layer height is the most important parameter. The smaller the layer height, the smoother curves will appear. Larger layer heights are better for bridging and overhangs. Smaller layer heights will also increase print time, as it will take more layers to complete the object. Infill density is the number that is expressed as a percentage. 0% will give a completely hollow print, while 100% will give you a completely solid object. We have found that 20% to 40% fill density is functional for most prints, in our case we use 100% infill because we do not use bottom and top layers. Your overall printing speed can be adjusted here. If no other speeds are determined in the later sections your printer will automatically default to this speed. The speed will be different, depending on what type of filament you are using. [10]

Analogue to the design, you could put support, this will usually occur when an object has an angle in relation to the build plate between 0 to 45 degrees. Or adhesion type to avoid adhesion issues causing your part to pop off at some point during the print. To fix this, use either Brim or Raft. Brim create a single layer of filament, contacting and surrounding your model. This will increase the surface area of the part contacting the build platform thereby preventing it from popping off the heated bed. Finally, Raft will generate a layer (it depends on the settings) of material underneath your object. Raft was more often used before the addition of heated plates to increase surface area.[10]

Moreover, the program indicates the size of the design so, you can change it in your liking. Finally, there is the possibility to view the design with multiple ways, to observe problems at the printing of it. Firstly, the overhang where it indicates points that the design may need support. Secondly, the ghost mode where the design becomes translucent to allow you to see what is behind it. Thirdly, Xray is very similar to Ghost mode. It will allow you to see into objects, ensuring that inner details are correct.[10]

3.1.1 Subtractive manufacturing

Subtractive manufacturing is term for various controlled machining and material removal processes that start with solid blocks, bars, rods of plastic, metal, or other materials that are shaped by removing material through cutting, boring, drilling, and grinding. There are many techniques analogue to the material and the accuracy that is needed: CNC machining (turning, drilling, boring, milling, reaming), Electrical discharge machining (EDM), Laser cutting, Water jet cutting.[26]

CNC stands for Computerized Numerical Control. It is a computerized manufacturing process in which pre-programmed software and code controls the movement of production equipment. CNC machining controls a range of complex machinery, such

as grinders, lathes, and turning mills, all of which are used to cut, shape, and create different parts and prototypes. It can subtractive a variety of metal, wood, plastic, ceramic, and composite material.[27]

Electrical discharge machining (EDM) is a metal fabrication process whereby a desired shape is obtained by using electrical discharges (sparks). Material is removed by a series of rapidly recurring current discharges between two electrodes, separated by a dielectric liquid and subject to an electric voltage.[28]

Laser cutting is a technology that uses a laser to vaporize materials, resulting in a cut edge. Laser cutting works by directing the output of a high-power laser most commonly through optics. The laser optics and CNC (computer numerical control) are used to direct the material, or the laser beam generated. The focused laser beam is directed at the material (thermoplastics, wood, acrylic, fabrics, metals), which then either melts, burns, ablate (this is the technique we use), vaporizes away, or is blown away by a jet of gas, leaving an edge with a high-quality surface finish. The resolution of these types of ablated induced surfaces can reach up to the diffraction limit.[29]

A water jet cutter is an industrial tool capable of cutting a wide variety of materials using an extremely high-pressure jet of water, or a mixture of water and an abrasive substance. The term abrasive jet refers specifically to the use of a mixture of water and abrasive to cut hard materials such as plastics, hard and soft metals, stone, glass, composites, while the terms pure waterjet and water-only cutting refer to waterjet cutting without the use of added abrasives, often used for softer materials such as wood or rubber.[30]

3.1.2 Fiber laser

Fiber laser is called like this because they are usually meant to be lasers with optical fiber as a gain medium. It consists of a diode pump which is typically operated between 915-980 nm, an optical fiber with glass silicate called cladding and a core doped with rare earth elements (erbium, ytterbium, neodymium, dysprosium, praseodymium, thulium and holmium) and at least Bragg gratings at the beginning and at the end of the core. [31]

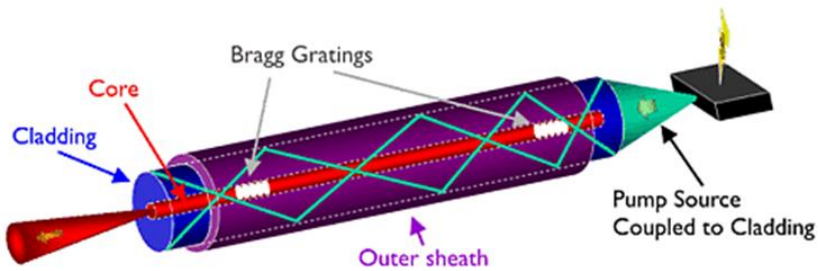

Figure 5: The set-up of the fiber laser[31]

To understand how it works, we need to understand first the Snell's law.

$$n_1 \times \sin\theta_1 = n_2 \times \sin\theta_2$$

Where the refractive index of the core is bigger than the cladding and if the angle of incidence is bigger than the critical angle of incidence, the light will be reflected with no refraction, this called total eternal reflection.

Furthermore, the most important thing is how the photon is created. First, it stimulates elements from the doped core from the ground state to a new with higher energy state (excited state). For Ytterbium laser (the one that we used) the energy source is typically of wavelength 976 nm. In most cases the electrons are in an unstable state and they will quickly move to a lower state which called meta-stable state. The electrons will stay in this state until they go back to ground state. So, many electrons are in the meta-stable state and wait for the right amount of energy to be stimulated into giving the energy up in the form of a photon. All it needs, is for one of the electrons to drop and emit a photon. Then, each of the photons will stimulate other electron to emit a photon, until we get a very large number of photons. This is called stimulated emission. Due to the way the photons are encouraging on another into existence, they are all in the same color and in step with each other, this is something that do not exist in nature. [31]

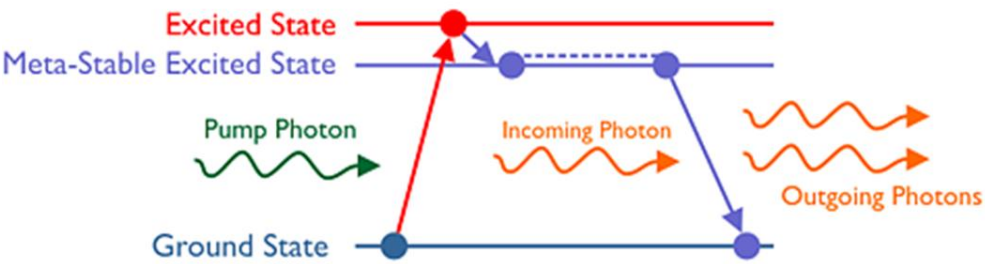

Figure 6: The way that the laser is created [31]

Moreover, these lasers have a fiber Bragg grating (FBG) which is a type of distributed Bragg reflector that is constructed in a short segment of optical fiber. An FBG is used as an in-line wavelength filter to block certain wavelengths or is used as a wavelength-specific reflector. A Bragg grating is simply a section of glass in a fiber which has stripes etched into the glass. With respect to fiber lasers, FBG's are used to create a cavity in the doped fiber which traps the Ytterbium or Erbium atoms and keeps them in the fiber core. Bragg gratings are used in fiber lasers as the wavelength reflector. At a very basic level, a fiber laser works by reflecting light through the optical cavity formed by the grating in a way that forces the photons to stimulate the Ytterbium atoms doped into the fiber. On both sides of the Yb doped "active" fiber, fiber Bragg gratings are placed which act as mirrors reflecting the light of the desired wavelength back and forth. The mirrors constitute a laser resonator. The desired wavelength of light is reflected selectively by the grating. This produces the induced emission in the resonator. This induced light then propagates in the resonator and is reflected by both FBGs to stimulate further induced emission. The repetition of induced emission

results in laser oscillation and ultimately the laser light is emitted from the output port which has the lower reflectivity grating.[32]

At least, Fiber lasers' have many advantages. Firstly, they are very stable because the beam is created inside the optical fiber, they do not have sensitive optics that need attention. Secondly, they have high beam quality because the beam is generated and confined inside the small core of the fiber. Thirdly, they can reach high powers compare to other lasers. At least, they are efficient and easy to cool. They could convert around 70-80% of the power put in by the pump source. So, less power is converted to heat and they could work in a wide range of environmental temperature and humidity.[31]

3.2 Combination of Fused Filament Fabrication and Subtractive technique

It is a common way to alter the surface of the 3D printed scaffold after is printed with subtractive manufacturing techniques.[60] The most well-known techniques used are either with laser (ablation, cutting) or with chemical etching. Although, with laser induced ablation or micromachining, you could abstract more specific, small designs up to the diffraction limit and use a variety of materials. Until now, they only alter the surface of the scaffolds and at some of them the second layer of them by changing the focus of the laser. In this way, you could alter the surface of the scaffold with designs more complex and smaller than the resolution of the printer or you could make it more porous. Below, two examples are described.

In the first example at figure 7, they ablated PLLA films with picosecond UV laser at different power analogue to the design. They made the PLLA film's surface rough, they also made grooves with width of 10 µm and depth 4 µm with two different spacing of 15µm(groove 1),25µm(groove 2) and two different microcavities circle and rectangle with depth 40 µm. The width of the grooves was close to the dimensions of human mesenchymal stem cells and the depth of microcavities is approximately 8 times the size of human mesenchymal stem cells. Figure 7, showed the cells morphology obtained by immunofluorescence confocal microscopy on four different PLLA surfaces (FLAT PLLA, ROUGH PLLA, GROOVES 1 and GROOVES 2) using cover slips as control. Immunofluorescent staining was used to examine cell cytoskeleton (phalloidin) and nuclei (DAPI) and focal adhesion points (vinculin) on these surfaces. Cell proliferation and adhesion were lower on the PLLA surfaces than on standard glass cover slips. Analysis of cell morphology showed cell alignment, both in terms of cell cytoplasm and nuclei, along the groove-patterned surfaces. In addition, substrate topography also affected cell nuclei orientation. [11]

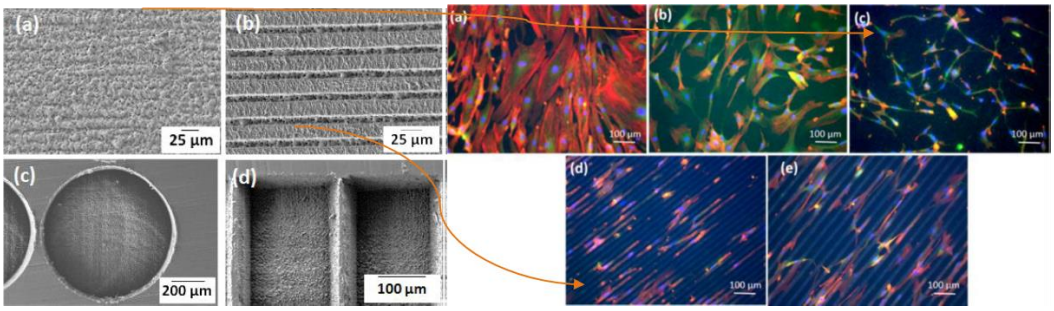

Figure 7: Different ablation designs with picosecond laser at PLLA films and MSCs cells culture for 14 days on a) tissue culture plastic b) PLLA flat c) Rough PLLA surface d) grooves 1 and c) grooves 2. Vinculin are showed in green, cell cytoplasm marked with phalloidin in red and cell nuclei marked with DAPI in blue.[11]

At last, they observed the differentiation of human mesenchymal stem cells on different surfaces, the expression levels of two adipogenic (ADIPO Q and CEBP_) and two osteogenic (RUNX2 and BMP2) specific genes on rough and grooved surfaces compared to flat PLLA were analyzed. Gene expression levels were measured on these surfaces considering four distinct culture conditions: growth medium (normal MSC culture medium), 100% adipogenic differentiation induction medium (Adipo), 100% osteogenic differentiation induction medium (Osteo) and 1:1 adipogenesis:osteogenesis induction medium (Mix). Analysis of adipogenic markers indicated that MSCs differentiated into adipocytes only when cultured in adipogenic or mixed media, however, no significant effect of surface patterns on cell differentiation into adipocytes was observed. A modest, although not statistically significant, increase of expression levels of these markers was detected in cells differentiating on grooves under adipogenic medium. In contrast, a significant increase in osteogenic marker expression was observed when cells were cultured in normal medium on patterns in comparison with FLAT PLLA. In addition, differentiation media did not further increase osteogenic marker expression on the patterned surfaces. These findings suggest that alterations on PLLA surface topography are enough to induce osteogenesis, independently of culture medium conditions. Furthermore, osteogenesis was favored over adipogenesis for all four surfaces (including FLAT PLLA) when cultured in mixed induction medium.[11]

The second example a combination of 3D FFF printer and the femtosecond laser with a galvanometric scanner and a linear motion stage. The differences with our set-up is that the 3D FFF printer is not combined with the laser. By changing the focusing, they can make ablated designs and in the second layer of the mesh.[12]

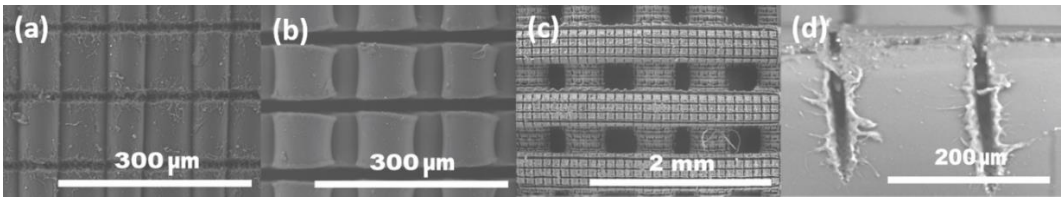

Figure 8: SEM micrographs of fabricated microgrooves in PLA employing a sharp focusing conditions: (a,b) sheet and (c,d) log-/wood-pile structure at different magnifications, front and side views, respectively.[12]

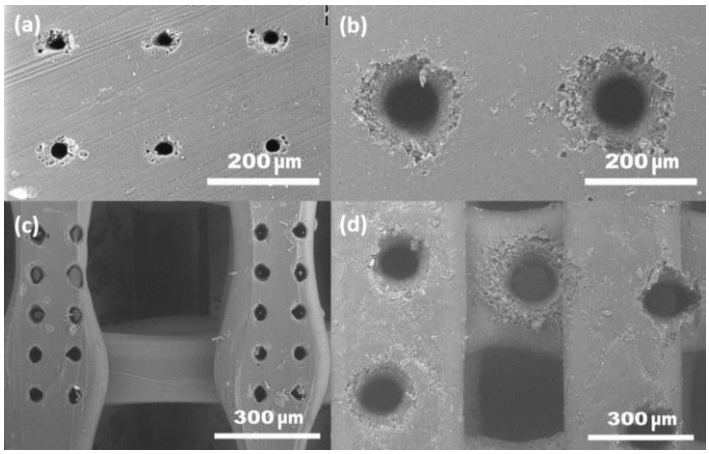

Figure 9: SEM micrographs of microholes drilled in PLA sheet (left) and woodpile (right): (a,c) using sharp focusing; (b,d) using FPF.[12]

Centimeter-scale microporous (pore size varying from 100 to 400 µm) woodpile scaffolds via thermal extrusion were successfully printed without sacrificial nor support structures required and can be used directly. Their structure geometry from macro to micro-scales were finely tuned by combining 3D printing parameters and femtosecond laser ablation employing sharp and filament focusing. 3D printed PLA log-/wood-piles were structured via laser ablation by making 5–10 µm width and 10–100 µm deep grooves, as well as 30–130 µm in diameter and 170–600 µm deep holes (aspect ratio of 4 to 5). It is shown in this work that much deeper and smoother holes could be made with light filament-assisted ablation. [12]

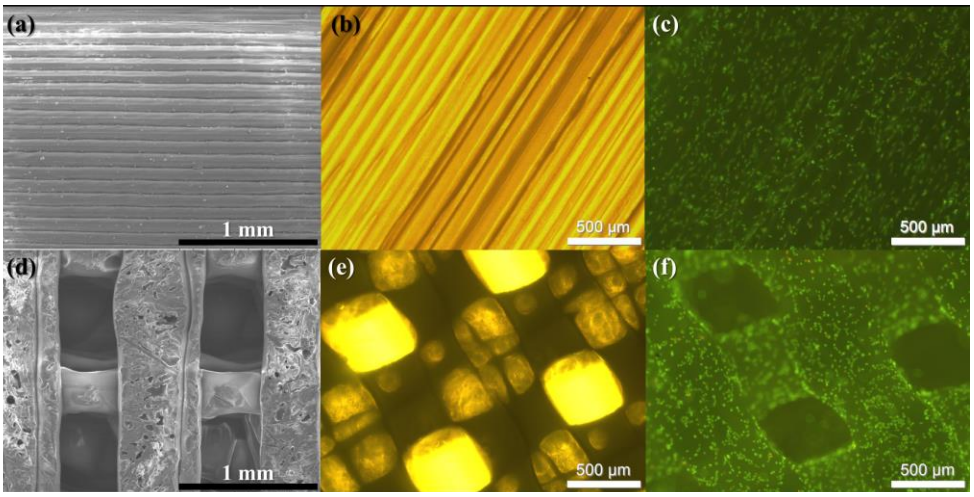

Figure 10: The SEM (a,d), light (b,e) and fluorescence microscope images (c,f) of the 3D printed scaffolds and myogenic cells grown on them: (top) 2.5D full-filled; (bottom) 3D microporous); in (c,f), cells are grown for 24 h and stained by an acridine orange-ethidium bromide mixture. Living cells are stained green, and dead cells are stained orange. The surface of the material is evidently biocompatible.

The scaffolds used in this work were 3D-printed out of PLA. Cell proliferation, viability and differentiation trends were studied. As evident in Figure 10, myogenic cells grown on the PLA scaffolds were alive, recognizable viable after staining with acridine orange and ethidium bromide; the green colour indicates viable cells. Fluorescence

microscope images show that the myogenic progenitor cells fully filled and homogeneously colonized scaffolds. It is known that the cell response to surface roughness is different depending on the cell type: for larger cells, the surface roughness could be correspondingly greater. They observed (the data are not presented in the article) that the muscle-derived myogenic progenitor cells differentiated into osteoblasts much more intensively on the porous scaffolds.[12]

Finally, in our occasion where we make an advanced combination of additive manufacturing and subtractive technique with laser. So, we managed to make designs that can cover resolution from 1µm to macro scale. We could construct ablated structures at any layer of the 3D scaffold (simultaneously as it printed) and more complex internal designs with laser, with smaller resolution than that of the 3D printer. At least, this combination is material impendent, quicker and cheaper than the other techniques.

3.3 Polymer-laser interaction

Laser is the acronym for "light amplification by stimulated emission of radiation", typically a high intensity beam of electromagnetic radiation. There are significant applications of laser in manufacturing sectors like laser beam milling, drilling, and etching. All of these lasers involved machining operations share a common phenomenon known as laser ablation. Laser ablation is a top-down process of removing material by focusing a laser beam onto a surface. Ablation occurs only when the material absorbs sufficient energy to be melted or vaporized. Ablation is a combination of both vaporization and melt expulsion as represented in Fig.11. When a focused beam of laser radiation strikes a surface, the electrons present in the substrate are excited by laser photons. This excitation results in the generation of heat by absorbing photon energy, which is consistent with Beer Lambert's law. Beer Lambert's law states that the amount of light absorbed is dependent on the thickness of the materials and intensities of the light source. The heating effects cause melting or vaporization of the material, thus resulting in the removal of macroscopic materials from the substrate. The transition from solid to gas results in the formation of a plasma plume. [13]

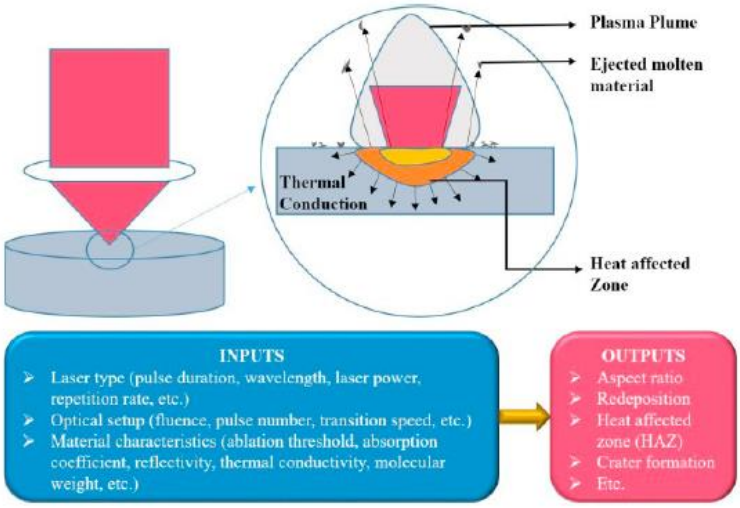

Figure 11: The mechanism at laser-material interface[13]

Interactions of laser radiation with polymers are greatly depending on the applied wavelength of the radiation. Generally, UV radiation causes photolytic breaking of molecular bonds within the material, while heat effects are limited. This breaking results in formation of free radicals, which can initiate photochemical reactions. Photons of IR radiation have energy insufficient for direct photolytic breaking of molecular bonds in most polymers. In the IR region, polymer functional groups are excited to higher vibrational and rotational energetic states that is accompanied by heat generation. A large accumulation of heat can lead to breaking of molecular bonds and thus to thermally activated reactions. When modified in the Vis range of electromagnetic spectrum, polymer materials are commonly doped with absorbing agents (photoinitiators) which decompose, initiating various reactions. Different characteristics of polymer absorptions depending on the wavelength of electromagnetic radiation are schematically presented in Figure 12.[14]

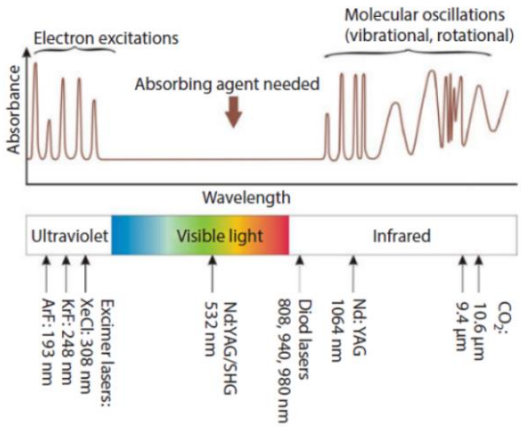

Figure 12: Polymer absorption depending on wavelength.[14]

In laser surface modification a very important parameter is energy (E_j) of radiation per unit area (laser fluence E_0) for a given polymer. The process of detachment of material fragments (ablation) starts when a certain value of laser fluence, the so-called ablation threshold, is reached or exceeded. Therefore, laser surface modification of materials is often classified as below or above ablation threshold.[14]

For the above reason, it was very important to find the Laser Induced Damage Threshold (LIDT) which is the lower limit at which an optic or material will be damaged by laser given the fluence, intensity and wavelength. It is a very important value because it determines the lower limit fluence.

This value can be found in an experiment either by single or multi shots. A single-shot test, also known as a 1-on-1 test, involves one shot of laser radiation on at least 10 different sample sites across an optical component with varying laser fluence. We have to measure the diameter of the spots, which are plotted as a function (eq.2) of fluence, and the data is linearly extrapolated to find where the damage probability is 0%, which gives the LIDT value. A multi-shot, or S-on-1, test differs from a single-shot

test in that it uses a series of laser shots, or pulses, per testing site as opposed to a single shot. The common number of shots per site, or S, is between 10 and 1000. Multi-shot tests provide a better prediction of the real-world performance of the optic.[33]

For a Gaussian beam, the spatial and temporal profile of the laser intensity is

$I(r, t) = I_0 \exp(-2r^2/\omega_0^2) \exp(-2t^2/\tau^2)$ (1)

where I_0 is the peak intensity at the center, ω_0 and τ are the spatial radius and temporal radius, respectively, at the $(1/e^2)$ intensity contour, r is the radial coordinate of distance from the propagation axis and t is the time variable.

The spatial distribution of the energy fluence

$E_r = \int_{-\infty}^{+\infty} I(r,t)\, dt = E_0 \exp(-2r^2/\omega_0^2)$ (2)

where E_0 is the peak fluence at the center of the beam. The peak fluence relates to the total pulse energy as

$E_{pulse} = \int_0^{\infty} E(r) 2p dr = \int_0^{\infty} E_0 \exp(-2r^2/\omega_0^2) 2\pi dr = \frac{\pi\omega_0 E_0}{2}$ (3)

Or

$E_0 = \frac{2x\mathrm{Epulse}}{\pi\omega_0^2}$ (4)

From equation (4), the peak fluence E_0 of the laser could be varied by changing the total pulse energy E_{pulse} or the spot size ω_0. [15]

Moreover, with the equation (2), we could extrude an equation for diameter because it is related with maximum fluence.

(2) $\Rightarrow \ln(E_r) = \ln(E_0)(-2r^2/\omega_0^2) \Rightarrow D^2 = \omega_0^2 \ln\left(\frac{E_0}{Eth}\right)$ (5) [16]

Laser processing of polymers involves complex physical phenomena. Laser-polymer interaction leads to photo-thermal or photo-chemical decomposition of polymers or both of them. Photo-chemical decomposition occurs if the electronic excitation due to the incident laser photons causes breaking of molecular bonds. Otherwise, it results in thermal excitation of the lattice. Photo-thermal decomposition considers the electronic excitation of photons to be thermalized which then results in the breaking of polymer bonds. Laser ablation of polymers depends on a variety of factors such as laser wavelength, repetition rate, fluence, and pulse duration. In addition, properties of the substrate materials such as thermal conductivity, absorption coefficient and reflectance play a major role. In our case, we use Ytterbium nanosecond fiber laser at 1064 nm. So, at this wavelength, the energy of the laser photon (approx. 1.16 eV) is much less than the energy bond of polymers, which are in the range of 3.8-11.2 eV. [17]For this reason, the laser-matter interaction is purely photo-thermal (multi-photon) and effects of photo-chemical decomposition can be ignored. In our case, we need above ablation threshold eq. 1 (for photo-thermal decomposition). When the material exceeds a certain value, called threshold ablation temperature (T_D), then the process of thermal ablation of the material begins.[14]

$$E_j^{th} = c_w \frac{(T_D - T_R)}{a(1-R)} \quad (6)$$

Where, C_w: specific heat of the material, TD: threshold ablation temperature, Tr: initial temperature, R: laser ablation reflection and a: coefficient of radiation adsorption.[14]

4.1 Mesenchymal Stem Cells (MSCs)

Stem cells are unspecialized cells with the capacity to self-renew and differentiate into a variety of cell types. They regarded to be the most vital biological components essential for growth, regeneration, embryonic development, and adult tissue maintenance.[48] Under certain physiological or experimental conditions, stem cells can be induced to become tissue or organ-specific cells having special functions, thus offer a source of precursor cells for treatment of degenerative, malignant and genetic diseases.[49] Mesenchymal stem cells (MSCs), a type of adult stem cells, can be isolated from almost all tissues and effectively expanded in vitro.[50] MSCs also called multipotent marrow stromal cells, are a heterogeneous population of cells that proliferate *in vitro* as plastic-adherent cells, have fibroblast-like morphology and form colonies *in vitro*.[17] MSCs can differentiate into cells of the mesodermal lineage, such as bone, fat and cartilage cells, but they also have endodermic and neuroectodermic differentiation potential.

MSCs, constitute a well-established cell source in tissue engineering because of their desirable characteristics, like ease of isolation from different tissues, rapid proliferation, multipotency and unique immunomodulatory properties. As aforementioned, they self-renew and differentiate into several lineages including adipocytes, osteocytes and chondrocytes. They have been isolated from various tissues and organs including bone marrow, adipose tissue, placenta, umbilical cord blood, the testes, the liver, the pancreas, the spleen, amniotic fluid, menstrual blood, dental pulp, the dermis and the lung. The source can be either human (adult or embryo) or animal origin.[21] In this particular work, mouse mesenchymal stem cells were used.

4.1.1 Osteogenic differentiation of Mesenchymal stem cells (MSCs)

Mesenchymal stem cells within their native environment in bone marrow, receive biochemical stimuli from surrounding cells. These stimuli likely influence how MSCs differentiate to become bone precursors. The ability of MSCs to undergo osteogenic differentiation is well established *in vitro*. However, the role of the natural cues from bone's regulatory cells, osteocytes and osteoblasts in regulating the osteogenic differentiation of MSCs *in vivo* are unclear.[46] Bone is constructed through three processes: osteogenesis, modeling, and remodeling. All these processes are mediated by osteoblasts, which work in tight cooperation with bone-resorbing osteoclasts. The osteoblasts synthetize the bone extracellular matrix (osteogenesis), and the osteoclasts carve out the shape to fit the physical environment (modeling) and adjust it to the demands of the body growth and the changing milieu (remodeling).[47] Osteoblasts are present throughout life, but their activity is highest during embryonic skeletal formation and growth. In an adult organism, osteoblasts are activated when there is need to regenerate a defect or when the bone matrix has been depleted. Osteoblasts secrete bone matrix proteins, including collagen type 1 alpha 1 (Col1a1),

osteocalcin (OC), and alkaline phosphatase (Alp). MSCs are the common ancestor for osteoblasts and can give rise either to myoblast, osteoblast, chondrocyte, or adipocyte lineages, depending on the current transcriptional regulators.[47]

Osteogenic differentiation of MSCs *in vitro* mainly depends on the culture conditions and, specifically, it is induced by the presence of dexamethasone, ascorbic acid and β-glycerol phosphate. Moreover, a key aspect of osteogenesis is the interaction of osteoblasts and their precursors with the matrix. Different modalities of mechanical stress can activate or inhibit regulating factors and therefore they can induce specific paths of osteogenesis. This makes it evident, that ECM plays a decisive role in the fate of MSCs, and consequently tissue engineering is the one about to offer scaffolds that are analogous to the natural bone.[47]

5.1 Mechanobiology

Cell behavior in vivo is influenced by a variety of extracellular signals. It is currently clear that many cellular aspects, including adhesion, migration, spreading, proliferation, survival, apoptosis, and gene expression, are modulated by interdependent signaling cascades of soluble signals, shear stresses, other supportive cells, and the nature of the extracellular matrix (ECM). Thus, the main challenge in and goal of tissue engineering is to mimic the features of the ECM and the surrounding environment of cells sufficiently so that cells function in the artificial medium as they would in vivo.[46]

Mechanobiology is an emerging field investigating the translation of physical forces into molecular biological signals. These forces can greatly impact cell behavior, countering or synergizing with other cellular signals from soluble factors. In the fields of tissue engineering and regenerative medicine, this fundamental knowledge is being translated to practical applications, but many challenges still remain. One of the hurdles is that the basic mechaniobiological machinery is fairly well established in 2D, but research in 3D is still in its early stages. In order to create functional tissues, cells need to be in a 3D environment.[19]

Mesenchymal stromal cells (MSCs) (the one that we used) are among the most widely used cell-type for tissue engineering as described above, and for mechanobiological studies because their multi-potent differentiation potential is highly dependent on mechanobiology.[19] This, potential pluripotent differentiation has been proposed to be mechanosensitive and is being investigated in different 3D scaffolds. However, no functional in vitro or in vivo differentiation of MSCs into lineage other than osteo-, chondro- or adipogenic, has yet been shown. Finally, an ideal scaffold for bone regeneration should be biodegradable, biocompatible, bioactive, osteoconductive and osteoinductive.[21]

5.1.2 3D Scaffolds' parameters that affect cellular behavior

5.1.2.2 Stiffness

3D hydrogels showed that their increased stiffness led to increased osteogenesis and reduced adipogenesis. The osteogenesis was observed on hydrogels around 20KPa, whereas the adipogenesis for 2.5Kpa. The upper stiffness limit is around 100KPa, this limit to substrate stiffness in 3D likely arises from a reduced ability for cells to remodel the matrix and gather adhesive ligands when encapsulated in hydrogels. In cases of 2D substrates, the matrix stiffness is enough on its own to guide MSCs differentiation. However, in 3D scaffolds it seems that cells need to be able to remodel the matrix sufficiently in order to build up the required cellular tension to undergo efficient osteogenic differentiation. This is likely also the explanation for the upper limit of substrate stiffness in the 3D hydrogels even though the hydrogels are non-covalently crosslinked, at higher stiffness the gels become less dynamic.[19]

5.1.2.3 Degradability

Khetan et al. added MMP-degradable peptides to covalently crosslinked hydrogels, so that the MSCs could remodel the matrix, almost all cells preferentially differentiated to the osteogenic lineage in 4.4 kPa gels[40]. Ferreira et al. also found that inhibiting hyaluronidase in 1 kPa degradable hyaluronic acid hydrogels inhibited osteogenic differentiation[41]. In type-I collagen gels, inhibiting membrane bound MT1-MMP (a collagen degrading enzyme) in hMSCs crippled degradation and osteogenic differentiation *in vitro* and *in vivo*[42], while enhancing adipogenic differentiation. Lastly, bone formation was enhanced *in vivo* in MSC-laden degradable alginate hydrogels, as opposed to more slowly degradable gels[43]. Even though not quantified, these papers demonstrate the importance of matrix degradation in 3D hydrogels to build up cellular tension and undergo osteogenic differentiation. In 2D, this does not seem to be of importance. Also, stiffness seems to be of subordinate importance in 3D, highlighted by efficient osteogenic differentiation in 1 and 4.4 kPa hydrogels if the gels can be sufficiently degraded. [19]

AT last, combinations of faster stress-relaxation and degradation of a 3D matrix could also result in even further enhancement of cellular tension, especially when done in a gel of optimal stiffness for a targeted cell differentiation lineage. How cells are cultured before such experiments is also important, as MSCs have been shown to have mechanical memory. When cultured on soft surfaces after pre-culture on stiff surfaces, MSCs preferentially differentiated to the osteogenic lineage. Without such pre-culture on stiff surfaces, MSCs efficiently underwent adipogenesis. [19]

5.1.3 Molecular mechanism of mechanosensing in 3D

Some effects of extra cellular properties are orchestrated by a machinery of mechanosensitive proteins. A cell adheres to the extra cellular matrix using integrins. Different combinations of α and β integrins can recognize different adhesion sites on extra cellular matrix (ECM) proteins, such as the widely used RGD-motif on fibronectin, or other motifs on other ECM proteins (for a specific integrin review thereader is directed to). When the integrin dimer binds to a ligand and force is applied, early focal adhesion proteins such as focal adhesion kinase (FAK), paxillin and talin, among others, bind to the intracellular part of the integrin subunits. This starts a cascade that will cluster integrins and recruit other proteins to the focal adhesions,

including zyxin, vinculin and actin filaments. When enough force is applied, these focal adhesions will mature into large protein complexes, creating a trans-membrane connection from the ECM, through multiple integrin dimers, to the actin cytoskeleton. Force on integrins is applied extracellularly, and/or intra-cellularly. An important force-generating element in cells are actin filaments with incorporated non-muscle myosin II (NM-II). Actin-myosin filaments join together to form large contractile bundles that exert force on the focal adhesions, creating tension in the cell. The actin-myosin filaments can be connected to two focal adhesions, or a focal adhesion and the nucleus. The cellular tension leads to changes in gene expression through a number of different pathways. Mechanosensitive transcription factors such as Yes-associated protein (YAP), transcriptional coactivator with PDZ-binding motif (TAZ), myocardin, related transcription factor (MRTF), and serum response factor (SRF), directly affect gene expression when translocated to the nucleus due to mechanical tension in the cell.[19]

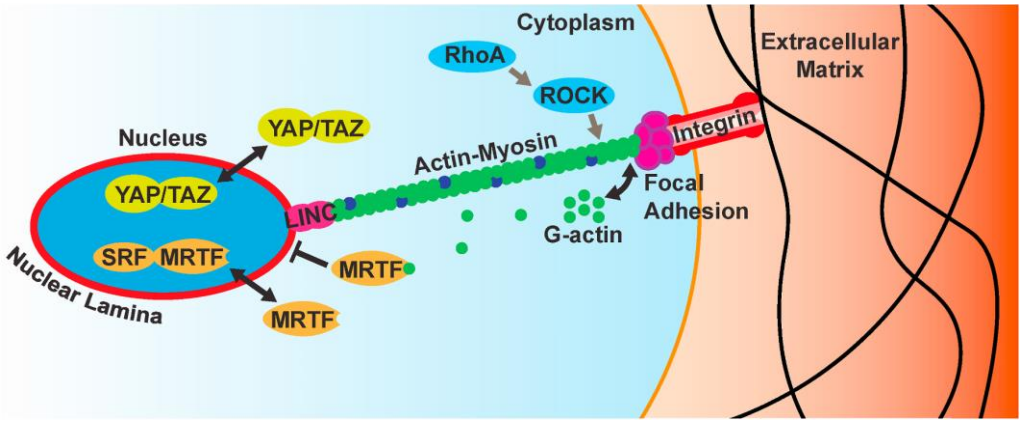

Figure 13: Overview of mechanotransduction pathways highlighted in this review. The interactions between these proteins have mainly been discovered in 2D and is now being investigated in 3D.[19]

5.1.3.1 Focal Adhesion

Focal adhesions are complex structures and consist of more than 60 different proteins that link the ECM-binding integrins to the actin cytoskeleton, of which some are mechanosensitive, and others are mechanotransducers. Focal adhesions play an important role in transducing mechanical signals from the outside of the cell to the inside. Important focal adhesions proteins, such as vinculin, which is the one that we use, focal adhesion kinase (FAK), paxillin, talin and zyxin, among others, all contribute to mechanotransduction. Vinculin knockdown decreased osteogenesis and increased adipogenesis. In line with this, inhibition of FAK inhibited osteogenesis in MSCs, osteoblasts and fibroblasts in 2D. Also, FAK has a signaling role for FAK in adipogenesis, rather than aiding in the build-up of cellular tension. Other proteins such as paxillin, zyxin and talin remain unexplored in their role in MSC differentiation in both 2D and 3D, even though they are likely to play an important role.

In 3D, there are often very few and small focal adhesions in MSCs and other cell types in contrary with 2D, but osteogenesis can still efficiently occur. Fraley et al.[44] have shown that this reduction in focal adhesions is a direct response to the 3D environment. Furthermore, creating protrusions and deforming the matrix is required to gather adhesive ligands in 3D, while it does not play a great role on stiff 2D substrates with plenty closely spaced adhesive ligands. This suggests a critical difference between the role of focal adhesions in 2D and in 3D. This difference is likely to translate more broadly to the build-up of cellular tension, and thus to proliferation and differentiation, although it needs further investigation.[19]

5.1.3.3 YAP/ TAZ

YAP and TAZ are a well-studied pair of mechanotransducive co-transcription factors that transfer to the nucleus upon high cellular tension in 2D. This nuclear translocation is regulated by two different pathways. One is phosphorylation, which increases nuclear export and degradation by the proteasome. The other is by direct force on the nucleus, opening nuclear pores and allowing YAP to move inside the nucleus by active transport. On 2D stiff substrates, where MSCs favor osteogenic differentiation, YAP is located in the nucleus. On soft substrates, YAP is predominantly cytoplasmic and MSCs favor adipogenesis. YAP has been directly involved in the differentiation of MSCs. Expression of non-degradable YAP or activation of TAZ inhibits adipogenesis and increases osteogenesis, while knockdown of YAP, TAZ or YAP and TAZ has the opposite effect. Also, bone specific YAP/TAZ knockout mice have severely impacted bone formation. Together, these papers clearly show an important role for both YAP and TAZ in differentiation of MSCs.

In 3D, YAP and TAZ have also been shown to be dependent on integrin, ROCK and actin-myosin. However, in 3D, as opposed to 2D, nuclear entry of YAP does not always correlate with adipo- or osteogenic differentiation of MSCs, while in other studies it does correlate. In 3D, osteogenic differentiation can still occur without pronounced nuclear translocation of YAP, adipogenic differentiation with mainly nuclear YAP, and different efficiencies of differentiations do not correlate with different levels of YAP. In summary, YAP and TAZ are not yet well studied in 3D tissue engineering, but the first results seem to reveal a similar function as in 2D.[19]

6.1 Characterization techniques

6.1.1 Scanning electron microscopy

A scanning electron microscope (SEM) is a type of electron microscope that produces images of a sample by scanning the surface with a focused beam of electrons. The electrons interact with atoms in the sample, producing various signals that contain information about the surface topography and composition of the sample. The electron beam is scanned in a raster scan pattern, and the position of the beam is combined with the intensity of the detected signal to produce an image. In the most common SEM mode, secondary electrons emitted by atoms excited by the electron beam are detected using a secondary electron detector (Everhart-Thornley detector).

The number of secondary electrons that can be detected, and thus the signal intensity, depends, among other things, on specimen topography. Some SEMs can achieve resolutions better than 1 nanometer.

6.1.2 How it works

The main SEM components include:

- Source of electrons
- Column down which electrons travel with electromagnetic lenses
- Electron detector
- Sample chamber
- Computer and display to view the images

In scanning electron microscopy, the electron beam scans the sample in a raster pattern. First, electrons are generated at the top of the column by the electron source. These are emitted when their thermal energy overcomes the work function of the source material. They are then accelerated and attracted by the positively charged anode. The entire electron column needs to be under vacuum. Like all components of an electron microscope, the electron source is sealed inside a special chamber to preserve vacuum and protect it against contamination, vibrations, and noise. Besides protecting the electron source from being contaminated, vacuum also allows the user to acquire a high-resolution image. In the absence of vacuum, other atoms and molecules can be present in the column. Their interaction with electrons causes the electron beam to deflect and reduces the image quality. High vacuum also increases the collection efficiency of electrons by the detectors that are in the column.[34]

To control the path of the electrons, they simply consist of coils of wires inside metal pole pieces. When current passes through the coils, a magnetic field is generated. As electrons are very sensitive to magnetic fields, their path inside the microscope column can be controlled by these electromagnetic lenses simply by adjusting the current that is applied to them. Generally, two types of electromagnetic lenses are used: The condenser lens is the first lens that electrons meet as they travel towards the sample. This lens converges the beam before the electron beam cone opens again and is converged once more by the objective lens before hitting the sample. The condenser lens defines the size of the electron beam (which defines the resolution), while the main role of the objective lens is to focus the beam onto the sample. The SEM's lens system also contains scanning coils, which are used to raster the beam onto the sample. In many cases, apertures are combined with the lenses to control the size of the beam.[35]

The interaction of electrons within a sample can generate many different types of electrons, photons, or irradiations. In the case of an SEM, the two types of electrons used for imaging are backscattered (BSE) and secondary electrons (SE). BSEs belong to the primary electron beam and are reflected back after elastic interactions between the beam and the sample. By contrast, secondary electrons originate from

the atoms of the sample; they are a result of inelastic interactions between the electron beam and the sample. Because BSEs come from deeper regions of the sample whereas SEs originate from surface regions, the two carry different types of information. BSE images show high sensitivity to differences in atomic number; the higher the atomic number, the brighter the material appears in the image. SE imaging can provide more detailed surface information.[35]

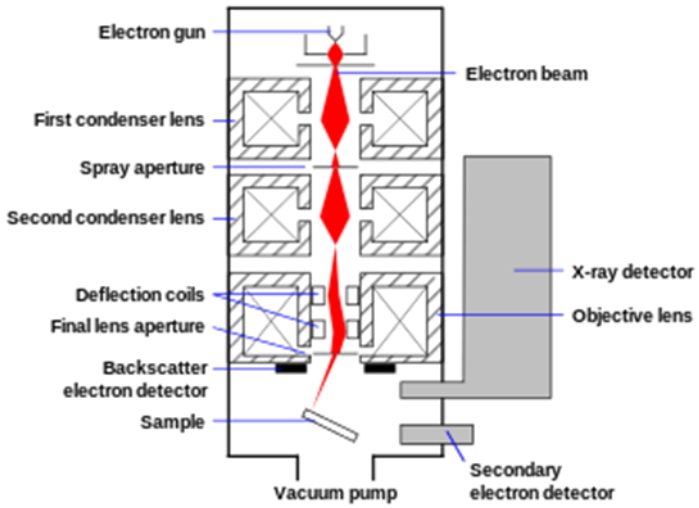

Figure 14: The set-up of SEM[34]

6.2.1 UV-Vis

Ultraviolet and visible spectrometers have been in general use for the last 35 years and over this period have become the most important analytical instrument in the modern-day laboratory. In many applications other techniques could be employed but nonrival UV-Visible spectrometry for its simplicity, versatility, speed, accuracy and cost-effectiveness.

Radiation is a form of energy and we are constantly reminded of its presence via our sense of sight and ability to feel radiant heat. It may be considered in terms of a wave motion where the wavelength, λ, is the distance between two successive peaks. The frequency, ν, is the number of peaks passing a given point per second. These terms are related so that:

$$c = \nu\lambda \quad (5)$$

where c is the velocity of light in a vacuum.

The full electromagnetic radiation spectrum is continuous, and each region merges slowly into the next. For spectroscopy purposes, we choose to characterize light in the ultraviolet and visible regions in terms of wavelength expressed in nanometers.

Other units which may be encountered, but whose use is now discouraged, are the Angstrom (Å) and the millimicron (mμ). 1nm = 1mμ = 10Å = 10^{-9} meters

The energy of a photon absorbed or emitted during a transition from one molecular energy level to another is given by the equation:

$$e=h\nu \quad (6)$$

where h is known as Planck's constant and ν is the frequency of the photon. We have already seen that $c= \nu\lambda$, therefore, $E= hc/\lambda$ (7).

When radiation interacts with matter, several processes can occur, including reflection, scattering, absorbance, fluorescence/ phosphorescence (absorption and re-emission), and photochemical reactions (absorbance and bond breaking). Typically, when measuring samples to determine their UV-visible spectrum, absorbance is measured. Because light is a form of energy, absorption of light by matter causes the energy content of the molecules (or atoms) in the matter to increase. The total potential energy of a molecule is represented as the sum of its electronic, vibrational, and rotational energies:

$$E_{total} = E_{electronic} + E_{vibrational} + E_{rotational}$$

The amount of energy a molecule possesses in each form is not a continuum but a series of discrete levels or states. The differences in energy among the different states are in the order: $E_{electronic} > E_{vibrational} > E_{rotational}$

By far the most common application in UV/Vis spectrophotometry is the measurement of liquids in cuvettes. However, high performance UV/Vis and UV/Vis/NIR instruments are more commonly used for materials characterization, which is an area dominated by solid samples. The figure 15 shows the various transmission and reflection modes for a clear solid sample. A transparent or semi-transparent sample can exhibit reflection, both specular and diffuse, and transmission, both specular and diffuse. The diffuse mode arises from particle scattering of the sample. Diffuse reflection is also called back-scatter, while diffuse transmission is called forward scatter and both are typically generated by rough surfaces. Specular reflection and transmittance are the product of non-scattering smooth surfaces. If a sample is opaque it can only produce diffuse reflectance or specular reflectance depending on its surface characteristics. The accessory of choice for solid samples is the integrating sphere. Integrating spheres are able to perform a variety of measurements on transparent, translucent, and opaque solid or liquid samples.

6.2.2 How it works

6.2.3 Measuring transmittance for a solid sample

In order to obtain a correct transmittance measurement for a solid, the possibility of the transmitted beam deviating in relation to the incident beam must be taken into account. There are a number of possible reasons for this deviation: refraction, uneven surface of sample, convex/concave surfaces. If the transmitted beam deviates considerably, there is a danger that part of it will not be fully picked up by the detectors. This will result in a reduced signal. The beam could also be diffused (light scatters inside the sample) in all directions by the sample, producing the same kind of

measurement error. Overall transmittance, i.e. linear transmittance plus diffuse transmittance (including any deviation of the beam), can only be measured using a specific item of equipment known as an integrating sphere. Alternatively, direct transmittance and diffuse transmittance can be measured separately.[38]

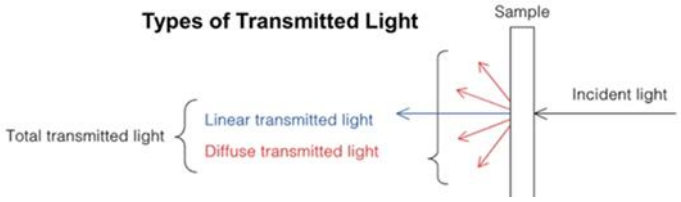

Figure 15: Types of Transmittance light[36]

6.2.4 Measuring reflectance for a solid sample

There are two kinds of reflectance, specular and diffuse. Specular reflectance refers to the part of the incident beam reflected at the same angle as the angle of incidence; mirrors typically produce specular reflectance when used as samples. Diffuse reflectance refers to the part of the incident beam reflected in all directions; powders produce diffuse reflectance when used as samples. Most samples produce a combination of specular and diffuse reflectance. Depending on the equipment used, it is possible to take separate measurements for specular reflectance, diffuse reflectance or overall reflectance. As with transmittance, an integrating sphere is needed to measure overall or diffuse reflectance. Specular reflectance is measured using other types of equipment specially designed for this purpose. Specular reflectance is particularly used when studying thin layer deposits.[37]

6.2.5 Measuring absorbance for a solid sample

The absorbance percentage is the same as the percentage of the incident beam absorbed by the sample, i.e. that part of the beam which is neither reflected nor transmitted. Absorbance can be calculated from the measurements taken for reflectance and transmittance by the following equation: %Absorbance=100%-%R-%T.[37]

6.2.6 Sample thickness

The sample thickness exceeds about 3 mm, the focal point will change considerably between baseline correction and sample measurement. This results in changes in the beam size at the detector light-receiving surface, making it impossible to obtain accurate transmittance values. This change in beam size results from the difference in refractive index between air and the sample. If the transparent sample is sufficiently thin, the change in beam size will be small and not cause any problems during measurements. As samples become thicker, this effect becomes more difficult to ignore. Total transmission measurements using an integrating sphere, as described below, are suitable for thicker samples. It is impossible to obtain accurate transmittance values for samples, such as lenses, which are thin but the focal point

changes significantly between baseline correction and measurement. Total transmission measurements are also suitable for these samples.[36]

6.2.7 Integrating sphere

The sphere is used instead of the standard detection module. The sample is placed against the sphere and the beam transmitted or reflected by the sample is reflected onto the internal reflective surface of the sphere before reaching the detectors inside the sphere (Figure 16). The sample is placed in front of the sphere if transmittance is being measured and behind it if reflectance is being measured. Note that in a typical scatter transmission measurement, only the transmitted and forward scattered light is collected by the sphere. The backward scattered (diffuse reflectance) light escapes collection. If both backward and forward scattered light need to be collected, then a center mount accessory can be employed. The center mount produces an absolute absorbance measurement and is very useful in measuring highly scattering or turbid samples on a 150 mm sphere.[36]

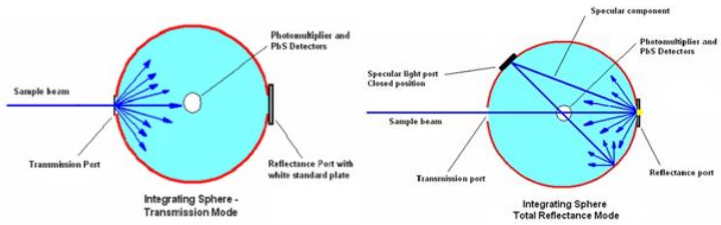

Figure 16: Diagram of transmittance and reflectance at the integrating sphere.[36]

6.4.1 Wettability

Wetting is the ability of a liquid to maintain contact with a solid surface, resulting from intermolecular interactions when the two are brought together. The degree of wetting (wettability) is determined by a force balance between adhesive and cohesive forces. Wetting is important in the bonding or adherence of two materials. Wetting and the surface forces that control wetting are also responsible for other related effects, including capillary effects.[40]

Adhesive forces between a liquid and solid cause a liquid drop to spread across the surface. Cohesive forces within the liquid cause the drop to ball up and avoid contact with the surface. The contact angle (θ) is the angle at which the liquid–vapor interface meets the solid–liquid interface. The contact angle is determined by the balance between adhesive and cohesive forces. As the tendency of a drop to spread out over a flat, solid surface increases, the contact angle decreases. Thus, the contact angle provides an inverse measure of wettability.[40]

A contact angle less than 90° (low contact angle) usually indicates that wetting of the surface is very favorable, and the fluid will spread over a large area of the surface. Contact angles greater than 90° (high contact angle) generally mean that wetting of

the surface is unfavorable, so the fluid will minimize contact with the surface and form a compact liquid droplet.[40]

For water, a wettable surface may also be termed hydrophilic and a non-wettable surface hydrophobic. Superhydrophobic surfaces have contact angles greater than 150°, showing almost no contact between the liquid drop and the surface. This is sometimes referred to as the "Lotus effect". For non-water liquids, the term lyophilic is used for low contact angle conditions and lyophobic is used when higher contact angles result. Similarly, the terms omniphobic and omniphilic apply to both polar and apolar liquids.[40]

6.4.2 High-energy vs. low-energy surfaces

Liquids can interact with two main types of solid surfaces. Traditionally, solid surfaces have been divided into high-energy and low-energy solids. The relative energy of a solid has to do with the bulk nature of the solid itself. Solids such as metals, glasses, and ceramics are known as 'hard solids' because the chemical bonds that hold them together (e.g., covalent, ionic, or metallic) are very strong. Thus, it takes a large amount of energy to break these solids (alternatively, a large amount of energy is required to cut the bulk and make two separate surfaces), so they are termed "high-energy". Most molecular liquids achieve complete wetting with high-energy surfaces.[40]

The other type of solid is weak molecular crystals (e.g., fluorocarbons, hydrocarbons, etc.) where the molecules are held together essentially by physical forces (e.g., van der Waals forces and hydrogen bonds). Since these solids are held together by weak forces, a very low amount of energy is required to break them, thus they are termed "low-energy". Depending on the type of liquid chosen, low-energy surfaces can permit either complete or partial wetting.[40]

Dynamic surfaces have been reported that undergo changes in surface energy upon the application of an appropriate stimuli. For example, a surface presenting photon-driven molecular motors was shown to undergo changes in water contact angle when switched between bistable conformations of differing surface energies.[40]

6.4.3 Wetting of low-energy surfaces

Low-energy surfaces primarily interact with liquids through dispersive (van der Waals) forces. William Zisman produced several key findings. Zisman observed that cos θ increases linearly as the surface tension (γ_{Lv}) of the liquid decreased. Thus, he was able to establish a linear function between cos θ and the surface tension (γ_{LV}) for various organic liquids.[40]

A surface is more wettable when γ_{LV} and θ is low. Zisman termed the intercept of these lines when cos θ = 1 as the critical surface tension (γ_c) of that surface. This critical

surface tension is an important parameter because it is a characteristic of only the solid.[40]

Knowing the critical surface tension of a solid, it is possible to predict the wettability of the surface. The wettability of a surface is determined by the outermost chemical groups of the solid. Differences in wettability between surfaces that are similar in structure are due to differences in the packing of the atoms. For instance, if a surface has branched chains, it will have poorer packing than a surface with straight chains. Lower critical surface tension means a less wettable material surface.[40]

6.4.4 Simplification to planar geometry, Young's relation

If the β phase is replaced by a flat rigid surface, as shown in Figure 17, then $\beta = \pi$, and the second net force equation simplifies to the Young equation.[40]

$$\gamma_{SG} = \gamma_{SL} + \gamma_{LG}\cos(\theta) \quad (8)$$

which relates the surface tensions between the three phases: solid, liquid and gas. Subsequently, this predicts the contact angle of a liquid droplet on a solid surface from knowledge of the three surface energies involved. This equation also applies if the "gas" phase is another liquid, immiscible with the droplet of the first "liquid" phase.[40]

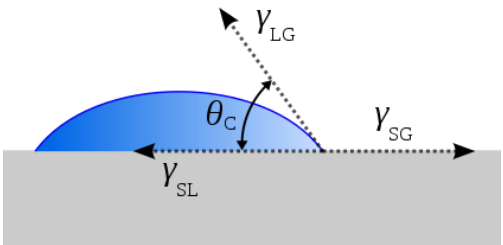

Figure 17: Contact angle of liquid droplet to a solid surface.[40]

6.5.1 Confocal laser Microscope

Confocal laser scanning microscopy (CLSM) is one of the most important advances achieved during recent decades in the field of fluorescence imaging and is considered as an essential tool in biological research. Compared with electron microscopy, CLSM procures much poorer resolution but requires considerably less specimen preparation and is compatible with three dimensional (3D) live imaging, enabling access to dynamic cellular and molecular processes. CLSM belongs to the family of photonic imaging technologies. Confocal means that the image is obtained from the focal plane only, any noise resulting from sample thickness being removed optically. Laser scanning means the images are acquired point by point under localized laser excitation rather than full sample illumination, as in conventional widefield microscopy. The basic concept of confocal microscopy was developed originally by Minsky in the 1950s. Egger and Petran produced the first mechanical scanning confocal laser microscope (a multiple-beam confocal microscope with a Nipkow disk) 10 years later. Advances in computer and laser technology enabled improvements to

the system, and the first commercial instruments became available in 1987. This technology has since become the technique of choice for a new generation of microbiologists interested in microorganisms spatially organized on surfaces, or biofilms.[22]

6.5.2 set up

CLSM is based on analyzing the fluorescence emitted by a sample after irradiation with a laser beam. Each fluorescent molecule is characterized by two characteristic spectra: (1) the excitation spectrum that corresponds to wavelengths that excite the fluorochrome, and (2) the emission spectrum corresponding to the wavelengths emitted by the excited fluorochrome. The latter is generally a mirror image of the excitation spectrum shifted to higher wavelengths. The distance between the excitation and emission maxima is called the Stokes shift. This must be greater than 20 nm if the excitation and emission wavelengths are to be separated correctly. The set-up is shown in the figure 18 and it consist of a laser source, two pinholes, an objective, a xy stage, a dichroic mirror, a scanner and the detector.[22]

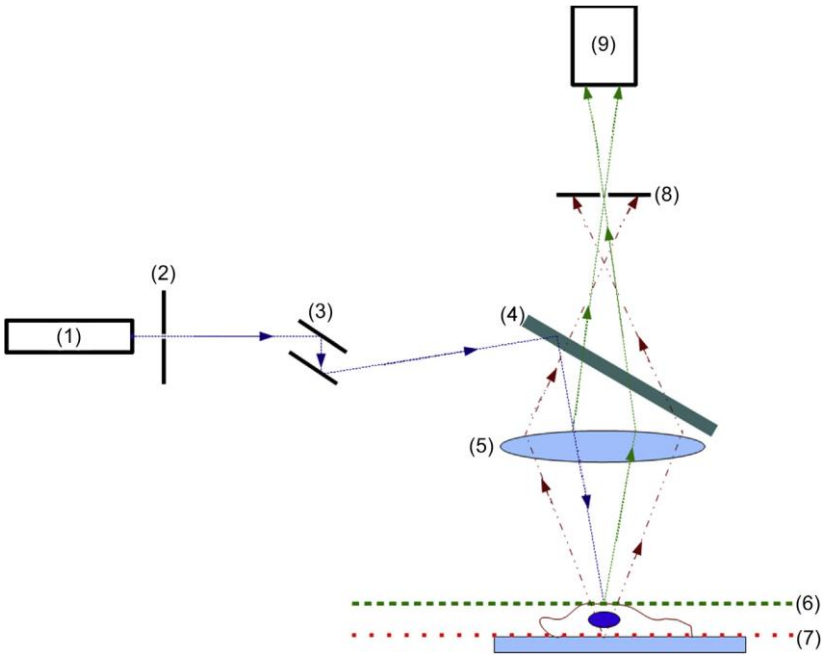

Figure 18: How does a CLSM works? A schematic representation of the optical pathway within a CLSM: A point source of excitation is produced by placing a filter (2) in front of a laser (1). Light then passes through a galvanometer-based raster scanning mirror system (3). A dichroic mirror (4) reflects incident light, and the lens of an objective (5) focuses it in the specimen. Light is reemitted in a superior wavelength and can pass through the dichroic mirror. A pinhole (8), placed in front of a detector (9), selects light that is mainly derived from the in-focus specimen field (6). Light from out-of-focus material (7) is diffuse when it reaches the pinhole, so that relatively little light from these fields reaches the detector.[22]

Lasers: Lasers enable greater penetration into thick specimens and exhibit a small spot of excitation at the focal plane that permits the equilibration of laser power and enables the preservation of the sample for toxicity and bleaching. This light source

displays some specific characteristics, such as monochromaticity (single wavelength), high directivity, temporal coherence to obtain a high concentration of energy in time, and spatial coherence to focus the laser beam onto a small area. Laser diodes mainly are used at present because they are more stable, robust, and powerful and because they take up less space. [22]

Pinhole: There are two pinholes, the one in front of the laser which focus the laser specifically and the second one is before the detector which cut out the unwanted fluences. Narrowing the pinhole can reduce markedly the optical section thickness and theoretically can improve resolution. As less light reaches the detector, however, higher gains on the photomultipliers (PMTs) are required, thus generating noise in the image.[22]

Scanner: The reason for the scanner is to change the direction of the laser light. The scanner is made up of two high-speed oscillating mirrors driven by galvanometer motors. Spatial position is determined by the position of the galvanometers (one mirror moves for the x lateral axis, the other moves in a y direction). A return of fluorescence emission through the galvanometer mirror system is referred to as descanning, and it remains in a steady position at the pinhole aperture. Scan speed can also be adjusted, but increasing the speed triggers a reduction in image resolution and photon counting and can increase shot noise. Manufacturers often use a frequency to define the speed of their scanner. [22]

Objective: The choice of objective is crucial to image quality and depends on the type of sample, the dye used, and the structural information required.[22]

XY stage: According to this Nyquist sampling theorem, optimal sampling is achieved when using voxel sizes that are 2.3 smaller than the smallest resolvable object in the sample.[22]

Detectors: The conventional detectors on commercial CLSM are PMTs. They detect light intensities but have no role in spatial localization. They are made up of vacuum electronics tube that convert photons in electrons. Amplification depends on the voltage (gain) applied to the PMT. The electrical signal ultimately is converted into pixels on the image. In practice, the gain and offset need to be adjusted such that in the final image, only a few pixels are fully black (background to zero) and fully white (maximum intensity Ó saturation, 255 in an 8-bit image).[22]

Experimental part

1.1 Set-up

In order to succeed the layer-by-layer print and ablation. An innovative machine was constructed, by combining the additive manufacturing and the subtractive technique.

More specifically the IPG Ytterbium picosecond fiber laser with a Fused Filament Fabrication technique. The laser is pulsed with pulse duration 0.15-5 ns, light wavelength 1064 nm, frequency 2-200 KHz and 0.10-30 Watts approximately. For the FFF mechanism, we used two different printers, the Lulzbot TAz 5 and the Creality Ender 3 pro.

At first, we had to combine the laser with the FFF printer with an optical path in order to be a combined machine. Then, we developed a software for this machine to work. The first set-up was with the Lulzbot Taz 5 printer where we printed a different base for the optics to be as close as possible to the nozzle. Although, this set-up had many disadvantages. Firstly, the base of the optics was not so stable because a part of it was on the air. For this reason, when the printer was moving, the base did a small oscillation. Secondly, the laser's ablation occured when the printers head moved. The printer's head moved with a belt, so the ablation was not so stable. At least, the printer's designs were not coherent because the printer head needed a change. More specifically, the nozzle was losing its temperature and filament was usually stuck.

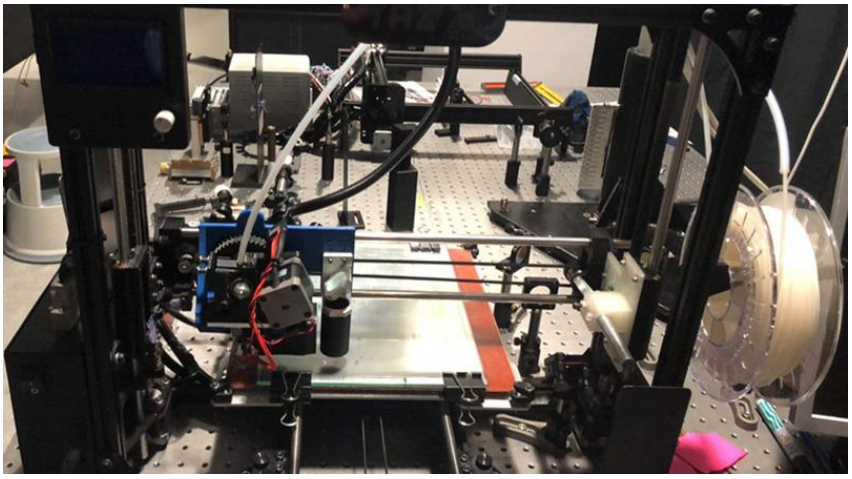

Figure 19: The first set-up

The second set-up was with the ender 3 pro and we constructed it more stable. The ender 3 pro printer had a different construction from the Lulzbot Taz 5 and it was easily changeable. At the new base the optics were behind the printer's head and more stable because the base was mounted to the printer's head and not in the air. So, when the printers head moved the laser had a smaller oscillation than the first set-up. At least, with the new printer the designs were more coherent. The disadvantages of this set-up were two. Firstly, the ablation speed was too low and secondly again for the ablation to occur the printer's head had to move.

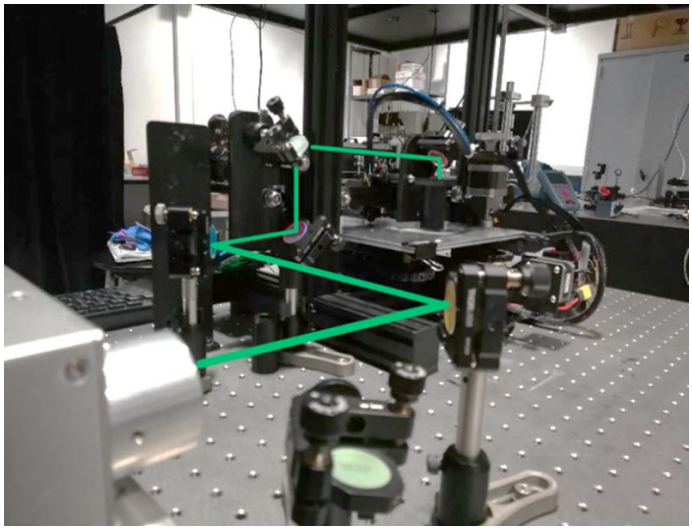

Figure 20: The second set-up

At the final set-up, we combined a small galvo scanner with the ender 3 pro printer and the Ytterbium picosecond fiber laser at IR region from IPG. We used this printer because it was easier to alter it. Also, we used a small, light Sino galvo to be held by the printer's motors**.** Galvo is a machine which consists from two mirrors that move mechanically in order to ablate the specific design. This galvo can ablate surface 10 by 10 cm^2. In order to be mounted behind the printer's head and to handle the weight of the galvo, we had to change all the set-up. At first, a second lead screw (with a stepper to drive it) was attached in order to handle the weight of the galvo and was connected with the z axis. Then, Mr. Ch.Doulias designed and printed 3D printed designs in order to keep the distance between the nozzle and the galvo fixed, so they can move simultaneously. At last, we made two metal parts in collaboration with the mechanical technical group of FORTH. The first one was to screw the mirror which send the laser light in the galvo and the second one was to fasten the galvo at the printer. The galvo and the above-described mirror have to move simultaneously, to direct the laser light into the galvo at every different Z height. With the final set-up we manage to have less vibrations, better resolution at the ablated designs and 100 times quicker ablation.

Figure 21: The final experimental set up that consists of a galvo scanner, an ender 3 pro, optical path and an Ytterbium picosecond fiber laser.

1.2 Software

For the above combinations to work, we needed to develop a software program. We had to design two sketches, one for the printer and one for the laser, where we translated them into stereolithography mode. Then, with the Cura program, we performed all the necessary changes in the designs before we translated them again into g-code. At last, we inserted these g-codes into the software where it combined them. For this reason, we could ablate the printer's design at each or at any layer we wanted.

The first program that Mr A. Lemonis developed, was for the first two set-ups. It was by LabVIEW and you could control the laser, the printer's functions, printer's bed, extrusion and the most important of all was the combination of the two designs.

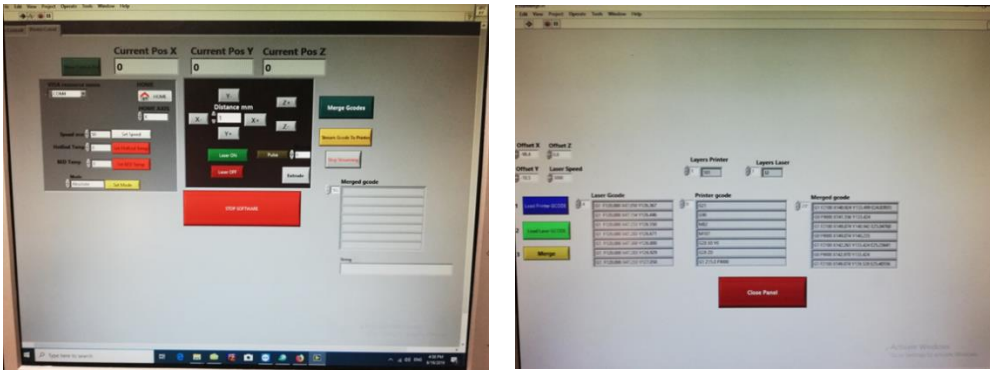

Figure 22: The first program

The second program that Mr. A. Lemonis developed, was for the last set-up. This time, he used python in order to be easily changeable and more functional. With this program we can control many functions. We could made circles, lines and spots only with galvo or we could only ablate designs with laser or we could only print or the combination of both. Moreover, we could do many changes in the laser's design. At first, we could minimize the design of the laser at xy axis. This was an important aspect because Cura could not recognize designs smaller than 0.7 mm. In this way, we could develop designs smaller than the resolution of the printer. Secondly, we could also multiply the minimized laser's design as many times as we wanted. We could not ablate small and large number of ablated designs with other due to the program. This was the reason why; we could not yet ablate lines. Thirdly, we could choose the layers that the laser ablation would start and stop so, we had the opportunity to ablate layer by layer at any layer we wanted. At last, Mr. A. Lemonis developed two windows with g-codes where we could control the laser's movement at z axis and the cleaning that the printer's head does when the laser ablation was occurred.

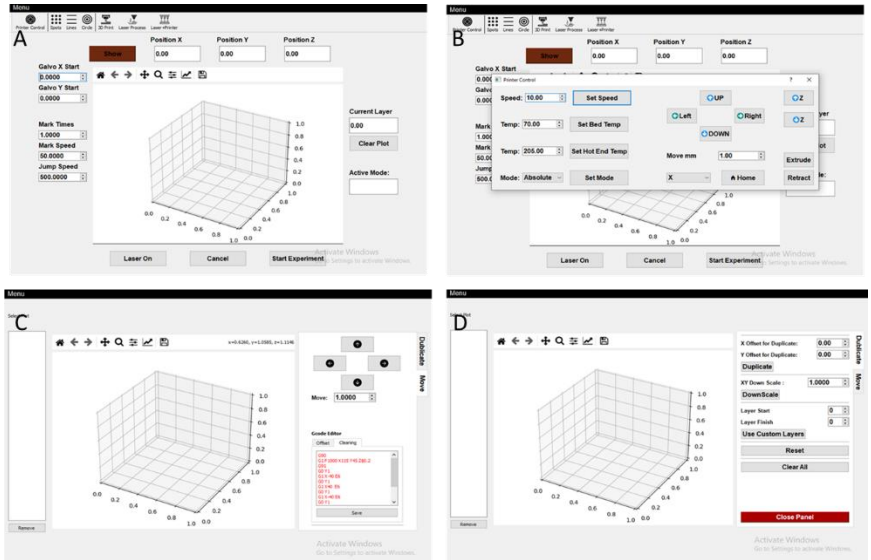

Figure 23: Custom-made program with Python for controlling the galvo scanner, the 3D printer and the combination of both. A) the main window B) control of 3D printer C),D) Insert the laser's, printer's or the both designs and we can move, duplicate, down scale and control the at what layers the laser will occur.

The last program that we used, was the laser's which was made in LabVIEW. In this program, we could control the laser's parameter more specifically the pulse duration (0.15,1,2 and 5 ns), the frequency from 2 to 200 KHz analogue to the pulse duration, the power of the pulse from 10 to 100% and if the laser will be controlled by this program (internal) or by another program (external).

Figure 24: The laser set-up

2.1 Experiments

As it discussed above, two set-ups were changed to end up to the final and best set-up. Many experiments and parametrics were occurred with the first two set-ups although, no significant result came out. Furthermore, the construction of the final set-up (as it is described in the above chapter) was been a big part of the master thesis. Also, the alignment of the laser was taken almost one month because many parts of the set up were in the air. This problem to be solved, a custom-made 3D

printed part was made. At last, after almost two months, the software was completed, only the layer-by-layer option had to be fixed.

Furthermore, the first complete experiment was made to proof the concept of the thesis. Although only surface ablation was occurred due to software problems. At first, meshes with 100μm space (figure 25) were made and then the surfaces were ablated with circles, lines and squares with laser parameters of 5ns, 5 KHz and 3.79 Watts. The circles (figure 27) were concentric with space between them 0.2 mm and total diameter of 6 mm. The lines (figure 28) had length 10mm and space between them 0.505 mm. At last, the squares (figure 26) had space between the squares of 0.2mm and total space of 10 mm. Then, MSCs were cultured by Dr. E. Babaliari on the above scaffolds in order to check their biocompatibility.

By then, the software program was completed, and experiments were started with laser parameters that have been found earlier. Unfortunately, none of these parameters worked for many layers. For this reason, another parametric was held for one layer with 0.15 ns, 1 ns, 2 ns and 5ns pulse duration, 2,5,10,30 KHz repetition rate, percentage of power 100-10% per 10%, mark time 5, speed 20,40,50,70 and 100 mm/sec. The best parameters for one layer were kept and were tasted for 22 layers. The best of the parameters are shown in the table below.

pulse duration	Repetition rate	Percentage of power	Mark time	Speed(mm/sec)
5ns	5KHz	80	5	70/50
5ns	5KHz	90/80	5	100
5ns	10KHz	90/80	5	100
5ns	10KHz	80	5	70
5ns	2KHz	100/90	5	100
5ns	2KHz	90	5	70
5ns	2KHz	90	5	50

Table 4: Parametric of laser at 22 layers of natural PLA.

Then, the laser induced damage threshold (LIDT) had to be found, which is a very important parameter as it described in corresponding chapter of the theoretical part. Spots were made with 5ns, 5KHz, from 100% to 10% laser parameters at 23 layers and 1 layer of natural PLA, to be also observed the role of the thickness. Diagrams were made with the diameter of spots (figure 29) and Fluences. The fluence of each spot was calculated with the equation 4. In addition, the diagrams were made with the information at the theoretical part, the function (5) and linear fitting. Below, it is described how the threshold fluence was calculated from the liner fitting:

$$\left.\begin{array}{l} Y=ax+b \Rightarrow a=2\omega_0^2 \\ b=-2\omega_0^2 \ln(F_{th}) \end{array}\right\} \Rightarrow \ln(F_{th}) = -b/a \quad [7]$$

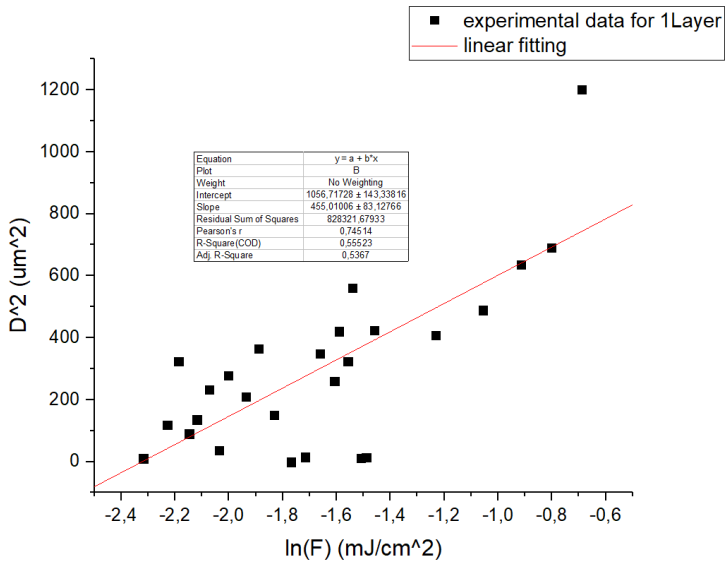

Figure 30: Diagram for LIDT for 1 layer height.

From the linear fitting of the diagram was concluded that the **F_{th}= 0.0981 mJ** (23% power).

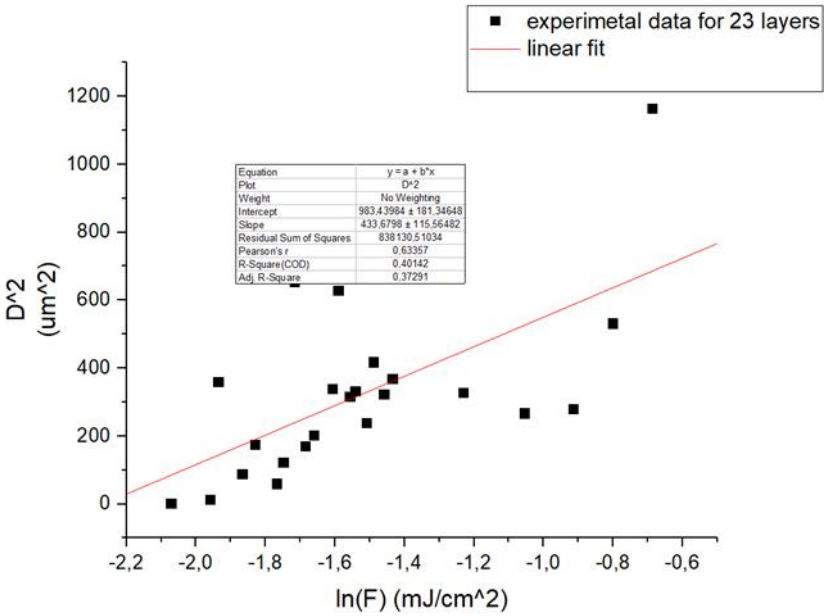

Figure 31: Diagram for LIDT for 23-layer height.

From the linear fitting of the diagram was concluded that the **F_{th}= 0.1036mJ** (24% power). Where no spot was seen in this power with the SEM.

The expected linear experimental data morphology was not shown in the above diagrams, because fluctuations at the diameter of the craters were existed. This may be caused by the roughness of the samples. So, the experiment will be repeated. At

last, from the diagrams above thickness is seemed to be played a marginal role at the LIDT. Nothing similar was found in the bibliography to be compared. Although based on two scientific articles [23] [24]:

1. F_{th}= 1.37 J/cm^2 for λ=800nm, τ=35fs, ω_0= 222.86 um, R.R = 1KHz and F=0.7 -3 J/cm^2 [23]

2.F_{th}= 5.5 J/cm^2 for τ= 6ps, λ=800nm, ω_0= 42 um, R.R = 1MHz and F=0.1-7 J/cm^2 [24].
Two conclusions had been made in this article firstly, for single shot the crater morphology and damage are depend on the pulse duration. Secondly, the pulse duration is reduced analogue to laser fluence.

Finally, new designs were constructed to be the final scaffolds for tissue engineering. One out of four designs was not successful (figure 32). A mesh was been the first scaffold with distance between lines of 0.25mm and 9 holes of diameter 0.7 μm had been ablated on the surface (figure 34). The porosity was been the reason behind the first scaffold. The cells would be grown all over the surface due to the easier delivery of nutrition. A mesh was been the second scaffold with two different gaps 0.32 mm and 0.50mm between the lines, and 30 layer-by layer holes of diameter 0.7 μm were ablated on its surface (Figure 35). Two different gaps had been used in this article[24] because the regeneration of bone was occurred easier. An orthogonal was been the final scaffolds with 3 different depths of ablated microcavities 0.15, 0.45 and 0.90 mm and 2 different dimensions (0.5x1) and (1x2) mm (Figure 36,37). In this scaffold, the cell growth was wanted to be observed analogue to the depth of microcavities. At last, the bigger microcavities were made for the cells to be cultured inside them.

Main objectives of the thesis: 1. The innovative combination of the additive manufacturing and subtractive technique. 2.The construct of 4D scaffolds with lower resolution than the 3D printer. 3. To set-up a cell study with the PLA meshes and MSCs at various time points in order to investigate the material's stiffness, 3D structure on the adhesion, proliferation, migration and differentiation of the cells.

2.2 Experiments and preparation of MSCs

2.2.1 Cell cultures

For all cell cultures at this study, Mesenchymal Stem Cells (MSCs) C57BL/6 from mice bone marrow were used. MSCs were grown in cell culture flasks using Dulbecco's modified Eagle's medium (DMEM) – low glucose (1000mgr/L glucose) supplemented with 10% fetal bovine serum (FBS) and 1% penicillin/streptomycin solution (PS) at 37°C in a 5% CO2 incubator, with medium renewal every 3-4 days. MSCs used for the experiments have a passage, ranging from 7-10. PLA meshes were UV sterilized and transferred into sterile wells of 12-well and 24-well plates. 50.000 -100.000 cells/ml in culture medium were seeded on the samples and were cultured for various time points. Tissue culture plastic (TCP) coverslips were the control samples (reference

material) in all the experiments. Table 1 summarizes the different time points and the specific experimental conditions per cell study.

Cell study on proliferation, morphology and mechanotransduction of the PLA meshes	**Cell study on adhesion, proliferation and morphology of the PLA meshes**	**Cell study on proliferation, morphology and osteogenic differentiation of the PLA meshes**
MSCs (50.000 and 100.000 cells/ml or per sample) **Time point:** 2, 4 and 7 days **Samples:** TCP Control, PLA flat (3D), 4D PLA meshes with 9h, 28h and 30holes, 3D PLA (bulk) with rectangular ablated areas of different depth **Main objective:** To investigate the effect of these meshes on cell adhesion, proliferation and differentiation towards osteogenic lineage	MSCs (100.000 cells/ml or per sample) **Time point:** 1 and 3 days **Samples:** TCP Control, PLA flat (3D), 4D PLA meshes with 9h, 28h and 30holes **Main objective:** To investigate the effect of these meshes on cell adhesion and proliferation	MSCs (50.000 cells/ml or per sample) **Time points:** 2syn11days & 3syn6days & 3syn14d & 3syn17d *with osteogenic differentiation medium* **Time points:** 13days & 16days & 23d **without osteogenic differentiation medium** **Samples:** TCP Control, PLA flat (3D), 4D PLA meshes with 9h, 28h and 30holes **Main objective:** To investigate the effect of these meshes on cell proliferation and differentiation towards osteogenic lineage
ImmunoStaining procedure for observation under Confocal Microscope: DAPI for cell nucleus (cell proliferation), Actin Phalloidin @568nm for cytoskeleton (cell morphology) and YAP/TAZ @ 647nm for cell mechanotransduction.	**ImmunoStaining procedure** for observation under Confocal Microscope: DAPI for cell nucleus (cell proliferation), Actin Phalloidin @568nm for cytoskeleton (cell morphology and orientation) and Vinculin @ 488nm for cell adhesion	**ImmunoStaining procedure** for observation under Confocal Microscope: DAPI for cell nucleus (cell proliferation), Actin Phalloidin @568nm for cytoskeleton (cell morphology and orientation) and Osteopontin (OPN) @ 647nm for Osteogenic Lineage differentiation.

Table 5**:** All the specific experimental conditions per cell study are listed

2.2.2 Scanning electron microscopy: preparation of the biological samples -dehydration procedure

The MSCs growing on the PLA meshes and TCP samples were analyzed by the SEM Jeol JSM – 639 OLV. After each time point, the cells were fixed following a specific fixation protocol. The medium was removed from samples and they were washed twice with 0,1M Sodium Cacodylate Buffer (SCB) (pH = 7,4) for 5 min in 4°C. Then they were fixed with 2,5% glutaraldehyde (GDA) / 2,5% paraformaldehyde (PFA) in SCB fixative buffer for 30 min at 4°C. The samples were then washed twice (for 5 min each time) with 0,1M SCB at 4°C. The samples at dehydration phase were washed in graded series of 30%, 50%, 70%, 90%, and 100% EtOH for 10 min each at 4°C. Then, the samples were transferred into a chemical hood and immersed in hexamethyldisilizane (HDMS)/ EtOH (50:50) solution for 30 min and 20 min, then, in 100% HDMS for 20 min twice at 4°C. As a final step, HDMS was removed, and samples left to dry completely overnight at the chemical hood. Prior to electron microscopy examination, the samples were sputter-coated with a 15nm film of Au (BAL-TEC SCD 050).

2.2.3 Osteogenic differentiation

To induce osteogenic differentiation, one to three days after MSCs culturing as described above, the standard culture medium removed and the osteogenic medium added which consisted of DMEM - high glucose (4500mgr/L glucose), 10% FBS, 1% penicillin/streptomycin, 0,1 mM dexamethasone, 0,17mM L-ascorbic acid and 10 mM β-glycerophosphate. The osteogenic medium was renewed every three days in order to observe MSCs differentiation.

The time points studied were:

- 3+ 6 days with osteogenic medium
- 2+11 days with osteogenic medium
- 3+ 14 days with osteogenic medium
- 3+ 17 days with osteogenic medium

- 13 days without osteogenic medium
- 16 days without osteogenic medium
- 23 days without osteogenic medium

These are considered as early and middle-stage osteogenic differentiation, and one of the main osteogenic markers expressed at such time points is Osteopontin (OPN). For comparison purposes the time points without osteogenic medium were also investigated.

2.2.4 Immunocytochemical assay for confocal microscope observations

For this assay, the medium was removed from samples and they were washed twice with Phosphate Buffered Saline (PBS) 1x (pH = 7.4) for 5 min and then fixed with 4% paraformaldehyde (PFA) for 15 min at RT. After removal of PFA solution, the samples were washed again twice with PBS 1x and treated with Triton-X100 0,1% solution in

PBS for 5 min in order to permeabilize cell membranes. Then, the samples were washed twice with PBS 1x for 5 min and blocked using 2% Bovine Serum Albumin (BSA) in PBS solution for 30 min. Subsequently, the cells incubated with the first antibody overnight at 4oC. Next day, the cultured cells washed twice with PBS 1x and incubated with the secondary antibody and actin phalloidin 568 or 660 (1:500) for 2 h and then nuclear staining carried out by 4,6-diamidino- 2-phenylindole (DAPI 1:10.000 in PBS) at RT. The first and second antibodies used in the present study are summarized in Table 2. Both 1st and 2nd antibodies were diluted in 1% BSA in PBS 1x solution, at the respective concentrations. The samples were transferred on microscope slides for observation using a 'Leica SP8' laser scanning confocal microscope.

First Antibody	Second Antibody	Phalloidins
Vinculin (mouse) (1:300)	Anti-mouse 488 (1:600)	Actin Phalloidin 568 (1:500) and/or (1:1000)
YAP (rabbit) (1:300)	Anti-rabbit 647 (1:600)	
Osteopontin (rabbit) (1:500)	Goat anti-rabbit IgG 647 (1:500)	

Table 6: The first and second antibodies used for the various cell studies.

Results and Discussion

1.1 Results of Scanning electron microscopy

The figures 25,26,27 and 28 show the first experimental results from SEM where we ablated only the surface of the meshes. All the ablated designs were with the same parameters and the results showed that the lines have a width about 50 µm and depth about 67 µm, the circles have width about 37 µm and depth about 61 µm and finally the squares have a width about 36 µm and depth about 44 µm. We can observe that all the ablated designs are recognizable, and we manage to make lines at the center of each strap. Although, there is obvious melting on the surface of the meshes.

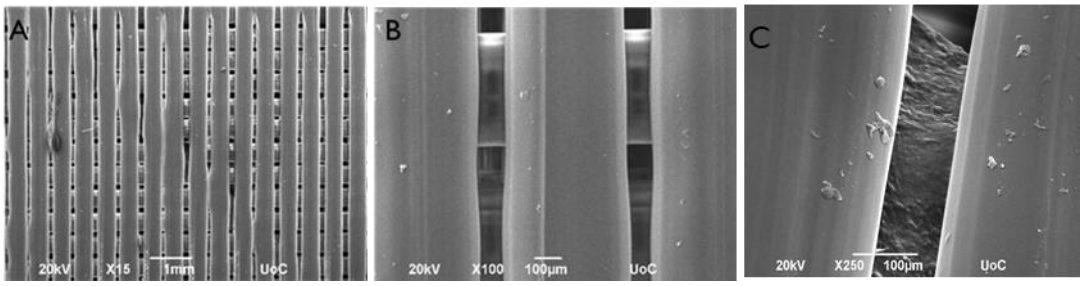

Figure 25: Top (A&B) and tilted @ 45°(C) view of mesh with 100 µm space.

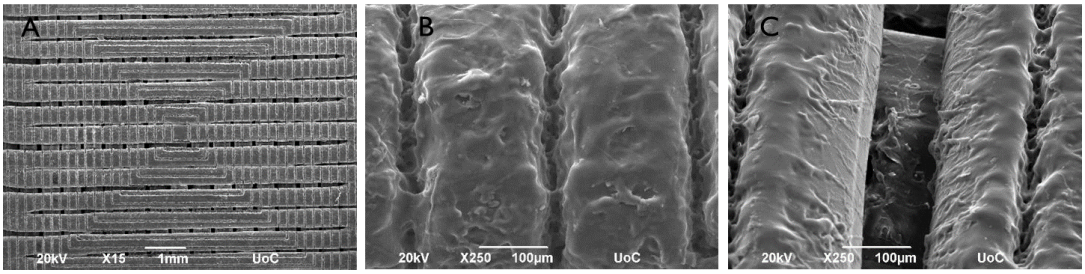

Figure 26: Top (A&B) and tilted (C) @ 45 º view of mesh with 100 µm space with ablated concentric squares 5ns, 5 KHz and 3.79 Watts.

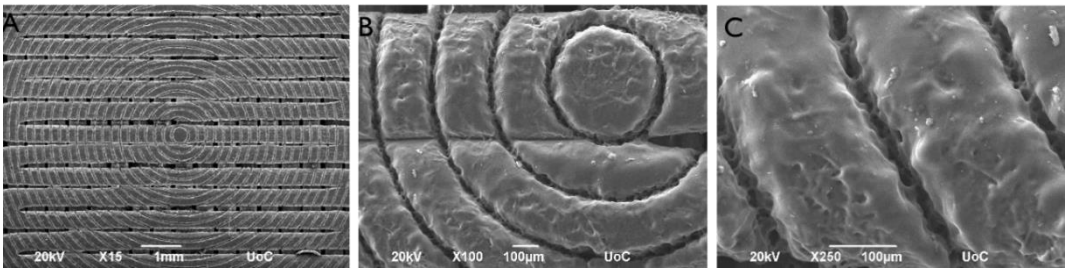

Figure 27: Top (A&B) and tilted (C) @ 45 º view of mesh with 100 µm space with ablated concentric circles 5ns, 5 KHz and 3.79 Watts.

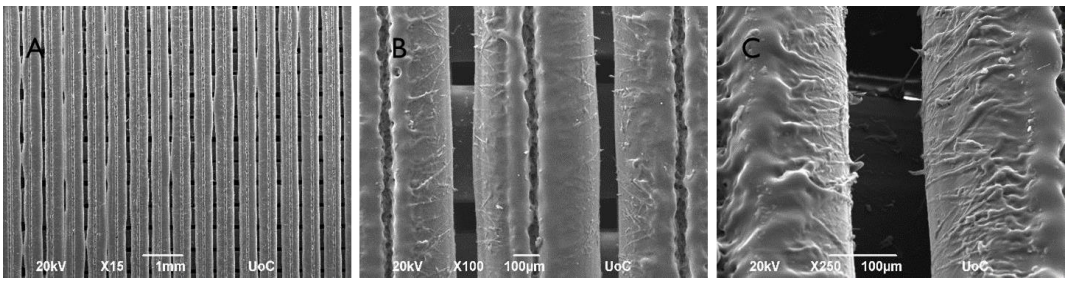

Figure 28: Top (A&B) and tilted (C) @ 45 º view of mesh with 100 µm space with line 5ns, 5 KHz and 3.79 Watts.

Figure 29 depicts the top view of SEM images of one spot (from many), with laser parameters 5ns, 5KHz, 1.88 Watts for 23 layers and 1 layer. This experiment showed differences in the shape, dimensions of the spots in different powers; the diagrams as presented above verified the hypothesis that the LIDT is different analogue to the thickness of our material.

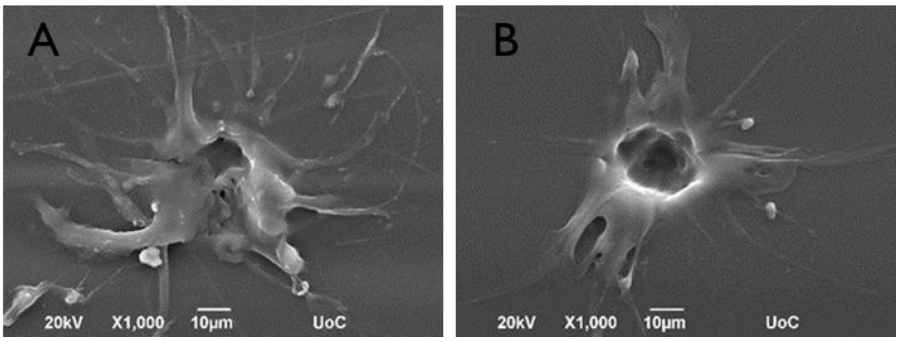

Figure 29: Top view of SEM images for 1.87Watts, 5ns, 5KHz 23 L(A) and 1 L(B) respectively.

Figure 32 shows the optimum scaffold but there were problems with the laser ablation. The square was 10x10 mm and the square holes were made by the 3D printer and had

distances 1x1 mm. The scaffold seems to have a sufficient shape, but the 3D printed gaps have excess of material. The scaffold was porous due to the design but smaller pores were desired with the laser ablation. However, it was impossible to achieve small and throughout pores although many attempts were performed.. For these reasons, we stopped using this scaffold and we used meshes which are easier to be produced and had smaller porosity.

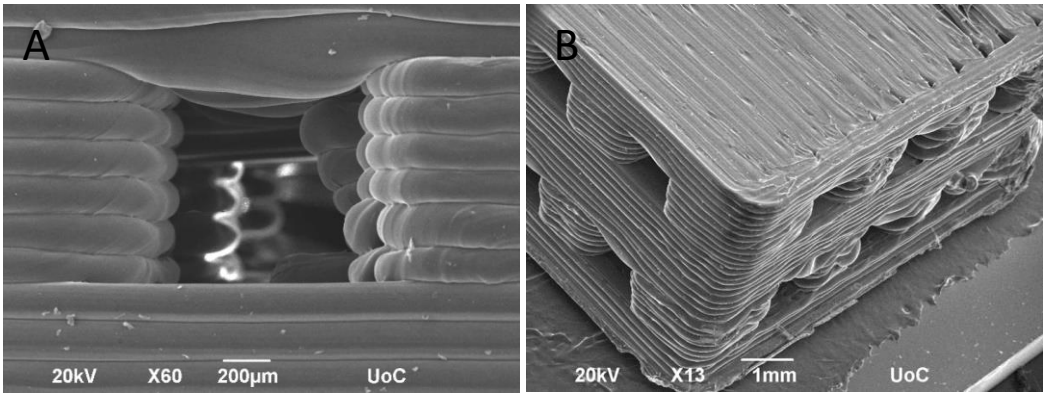

Figure 32: Top (A) and tilted(B) view of SEM images for 1.87Watts, 5ns, 5KHz 33 L and 1 L respectively.

Figure 33 depicts a simple square (10x10) with (B) and without (A) laser treatment. At the square with the laser treatment, we can observe that there are 16 holes of diameter 0.7mm, without a lot of melting at their edges. In addition, both designs have a smooth surface without gaps. These scaffolds were suitable for wettability and UV-Vis measurements.

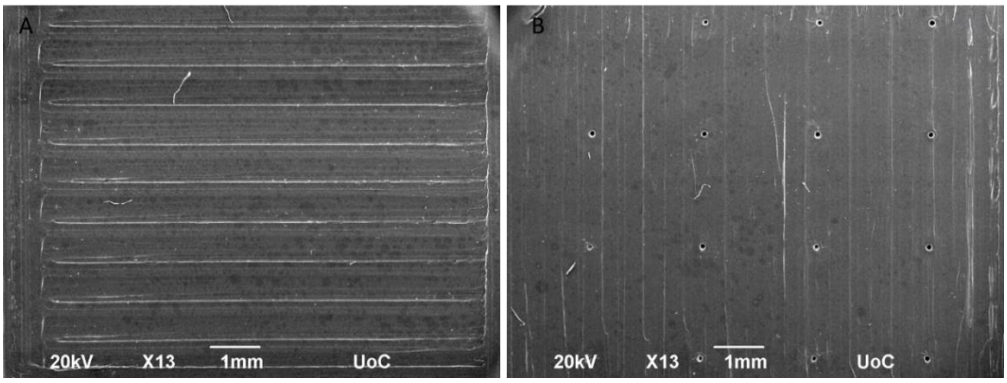

Figure 33: Top view of square (10x10 mm) A) and B) 16 laser ablated holes of 0.7 mm with laser parameters of 5ns, 2KHz and 1.91 Watts.

Figures 34,35,36 and 37 present the final scaffolds that I made for the cell culture studies. With the SEM, we observed the morphology of the whole scaffolds. The two first scaffolds were 10x10 with gaps 0.25mm and 0.32 and 0.50 mm respectively. Although, the gaps at the first scaffold seem to be incoherent. Moreover, the surfaces of the scaffolds are smooth, and the holes are not all the same size approximately 85µm, analogue to the depth of the hole. At last, the two orthogonal scaffolds (figure 36,37) look similar, but they have an elementary difference, the first one is smaller(10x5mm) than the second one is (10x8mm). Moreover, the ablated microcavities (rectangles) are of different size, at the first sacffold is 0.5x1 mm and at

the second one is 1x2 mm. The reasons for sizing up the scaffold were two. Firstly, the surface of the first scaffold has some gaps at the layers where the laser is occurred. This may be fault of the printer due to the small size of the scaffold (10x5 mm) or under extrude problem at these layers. Secondly, Dr. P.Kavatzikidou wanted to grow the MSCs cells only inside these ablated microcavities. Furthermore, we can observe that for both scaffolds the ablated microcavities are very clean, they do not have excess material at the sides, also there have not so much melted material outside the microcavities. The surface of the main orthogonal is smooth but with splashes of material on the surface. Finally, the ablated surfaces have a significant roughness due to the ablation, this may help the cells growth.

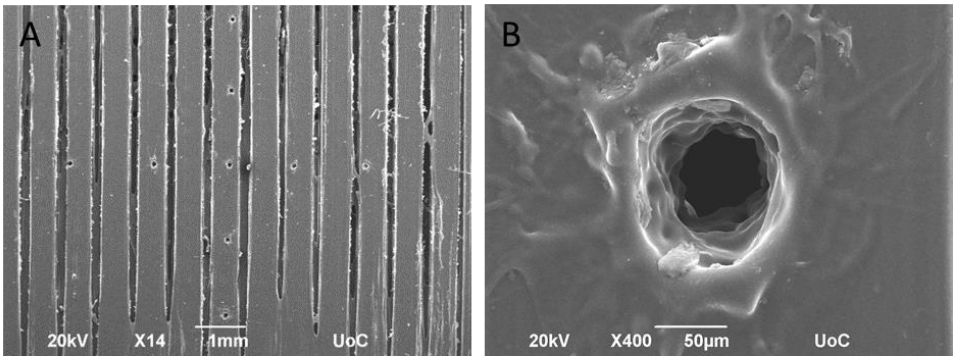

Figure 34: Top view of SEM images for a mesh with distance 0.24 mm and 9 laser ablated holes with 5ns, 2KHz and 1.91 Watts and diameter of 0.7mm.

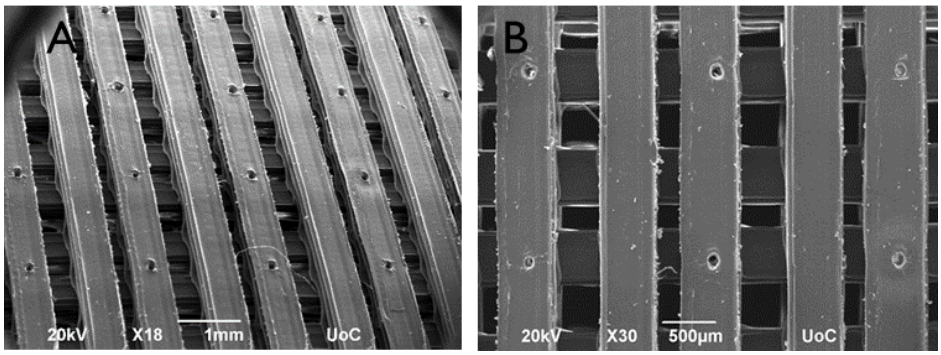

Figure 35: Tilted(A) @ 45 ^{o} and Top(B) view of SEM images for a mesh with distances 0.32mm and 0.50 mms and 30 laser ablated holes with 5ns, 2KHz and 1.91 Watts and diameter of 0.7mm.

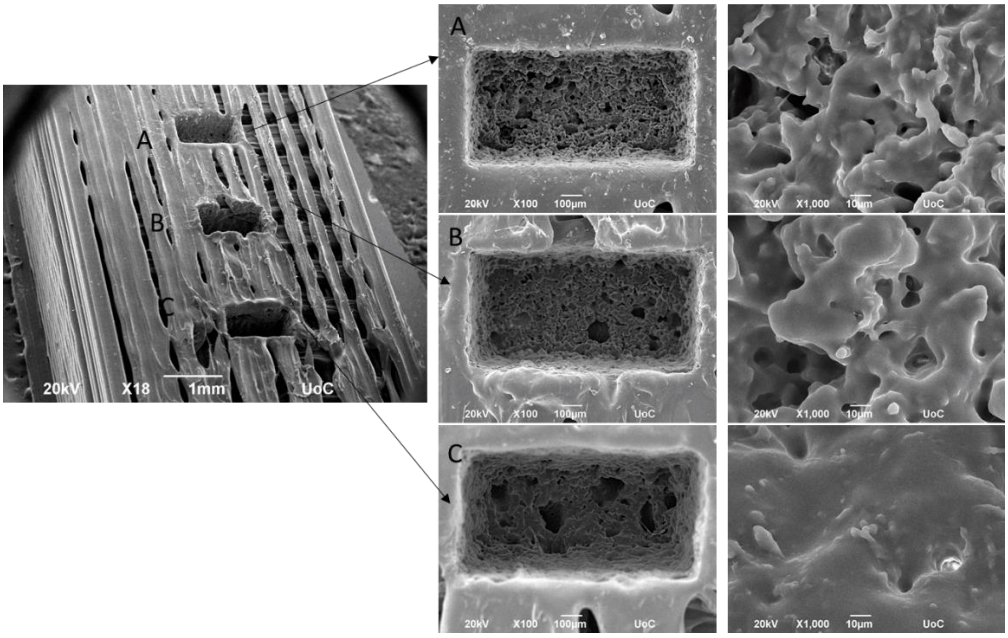

Figure 36: Top and tilted view @ 45 º of SEM images for orthogonal with 3 different depth of ablated microcavities (0.15(A), 0.45(B) and 0.90(C) mm) and distances 1x0.5 mm with laser parameters 5ns, 5KHz, 3,92 Watts, 100mm/sec and mark time =16.

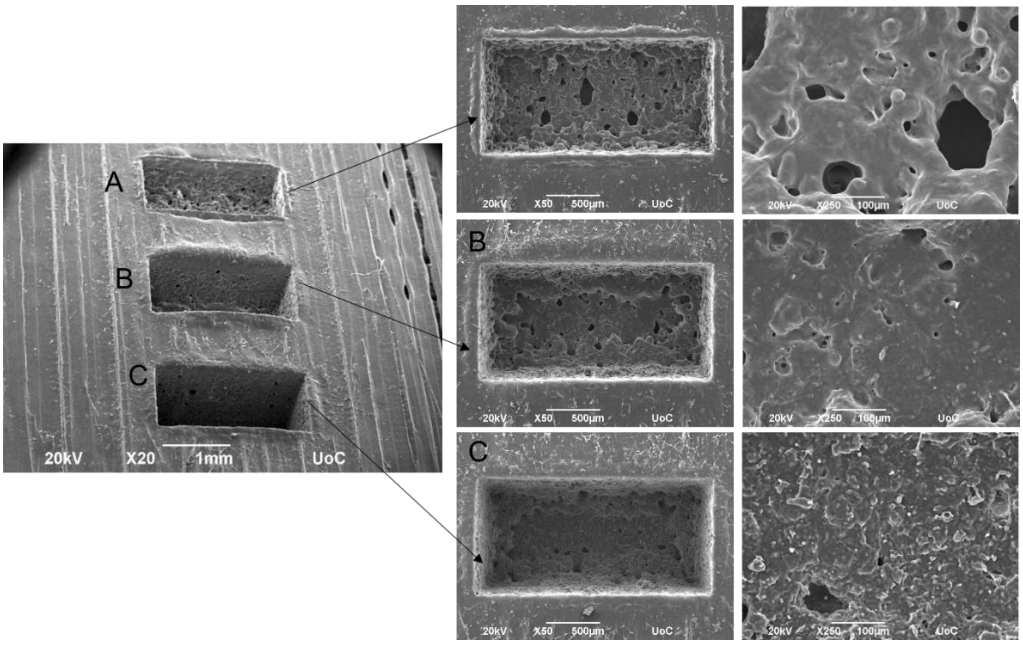

Figure 37: Top and tilted view @ 45 º of SEM images for orthogonal with 3 different depth of ablated microcavities (0.15(A), 0.45(B) and 0.90(C)mm) and distances 2x1 with laser parameters 5ns, 5KHz, 3,92 Watts, 100mm/sec and mark time =16.

1.2 Results of UV-Vis

In order to do the UV-Vis measurements I made some flat samples and with ablated holes to observe if there was a difference in the Absorbance of the material after the ablation. The first experiment was held out with the help of Ms. K. Argirou where we observe that the reflection was not right. At the calibration, the reflectance at black surface has to be below 8% although, it was almost 40% after 500nm. This indicates that the instrument has

a problem. However, we took the measurement of Transmittance and Reflectance for the flat PLA and the Absorbance came positive from the below equation: %A= 100%-(R+T).

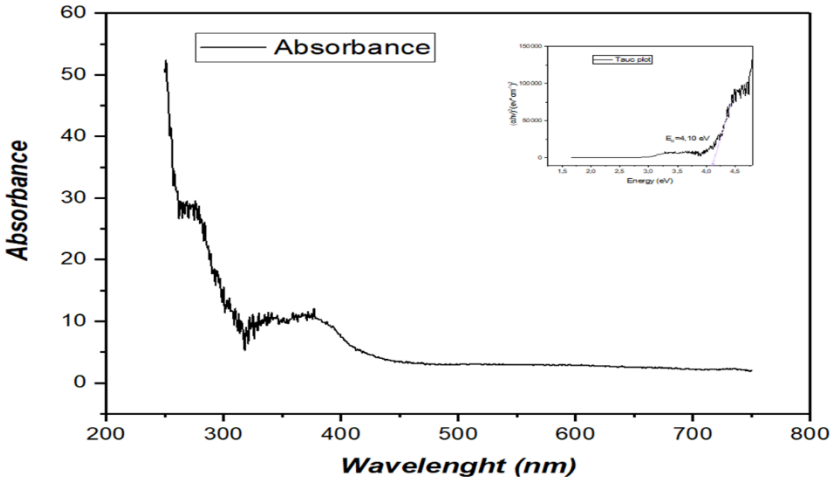

Figure 38: The diagram for flat PLA of Absorbance% to Wavelength and the second diagram is given by tauc plot exercise and it gives the energy gap.

From this diagram we can observe that the absorbance at this figure is around 375 nm which is not right based on the above bibliography, although there is noise at the peak.

By using two equations [hv=1240/nm (y axis) & hav=2,303*absorbance*hv)^2 (x axis)], I made another diagram and I found out that the energy gap of PLA based on the first diagram is around 4.10 eV. Although, from bibliography I found that the neat PLA is 3,3 ev but ours is a filament natural PLA and it may have a different energy gap. From the above results we can be almost sure that the instrument does not measure wright.

The second experiment was with the collaboration of Dr.P. Kavatzikidou, where again the Reflectance had more problem than before. We made the alignment better and again the Reflectance has the same problem, but it was lower than before the alignment. We took a reflectance at the natural PLA and the Absorbance came negative. So, we took again the measurement at black sample and at the white compact powder at the Reflectance and Transmittance at the white compact powder. The results were not good, the reflectance was increasing after 500 nm and the Transmittance after 380 nm (figure 39). We concluded that the measurements for the Reflectance and transmittance are valid above 500 and 380 nm respectively. Our peak is at 375nm approximately so, we could not take account the measurements for reflectance but only for Transmittance (figure 40).

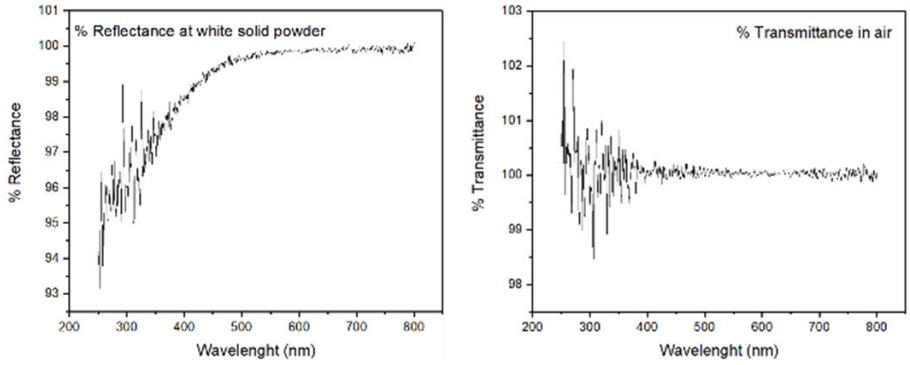

Figure 39: Diagrams of Reflectance and Transmittance taken with the white solid powder, the problems of the UV-Vis instrument are shown after 500 and 380 nm respectively.

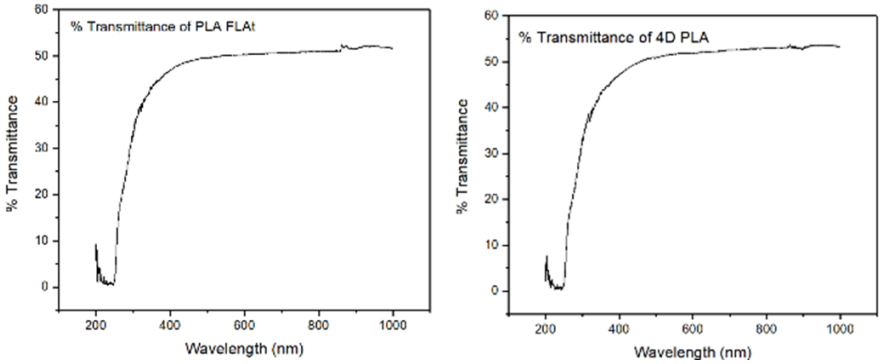

Figure 40: Diagrams of Transmittance of Flat PLA and 4D PLA.

From the Figure 40, we observed that the diagrams of flat PLA and the 4D PLA have almost the same behavior. We concluded that the transmittance of the material did not change over the laser ablation.

1.3 Results of Wettability

The wettability measurements were taken by Dr. S. Maragaki where she made two experiments, the one with 4uml and the second one with 8uml of water. They usually use volume from 2 to 10 µl because they do not want the weight of the water to play a role in the wettability. Both experiments showed that the PLA flat and 4D PLA (ablated with laser) have the same behavior. Both of them were hydrophilic because the angles were less than 90 degrees. However, a problem was occurred because with the 4uml droplet of water the 4D PLA (figure 41) was more hydrophilic than flat PLA although, with 8uml droplet of water (figure 42) the results were the opposite.

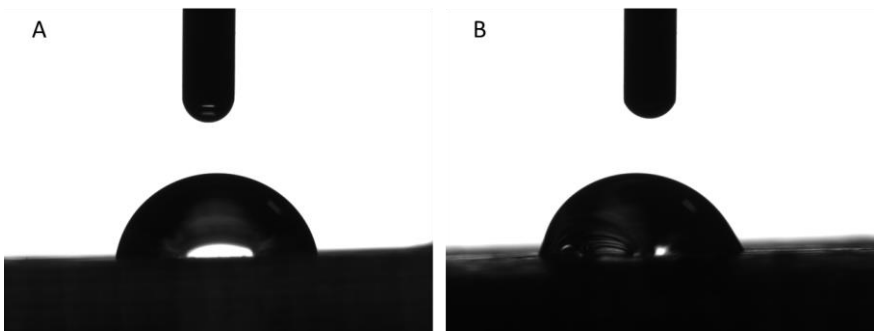

Figure 41: Pictures from wettability of 4µl droplet of water A) Flat PLA and B) 4D PLA.

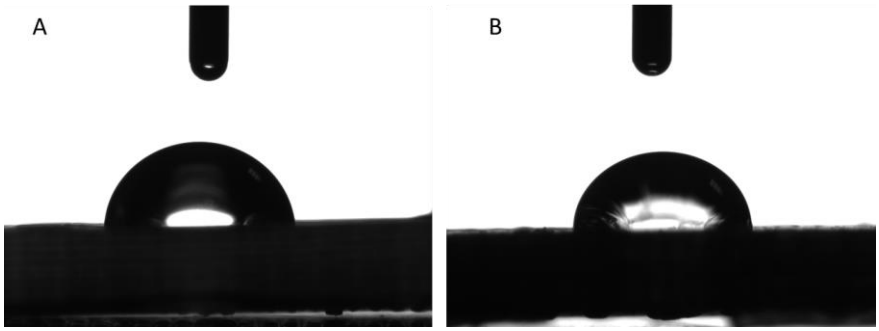

Figure 42: Pictures from wettability of 8μl droplet of water A) Flat PLA and B) 4D PLA.

Sketch	Contact angle (4ul)	Contact angle (8ul)
Flat PLA	77.86°	82.72°
4D PLA	73.89°	86.97°

Table 7: The contact angles of two different sketches and two different volume of droplets.

For both volumes, the materials are hydrophilic although with the bigger water droplet, they are closer to hydrophobicity.

1.4 Results of Cell Culture

1.4.1 Results of Scanning Electron Microscopy

In Figures 43,44,45 and 46, we can see the first experimental results with 100K MSCs for 2 days of culture. We can observe that the cells proliferated and attached well at all the scaffolds. We can observe that the MSCs also grow between the lines of the meshes, underneath, in particular the layer below and inside the ablated designs.

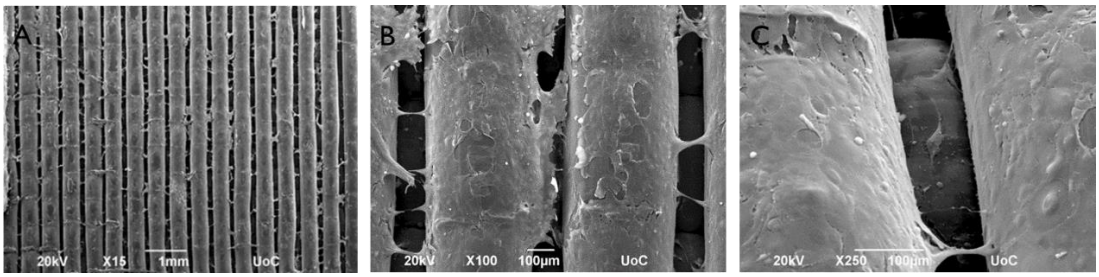

Figure 43: Top (A&B) and tilted (C) @ 45 º view of mesh with 100 μm space and for 2 days in 100K MSCs culture.

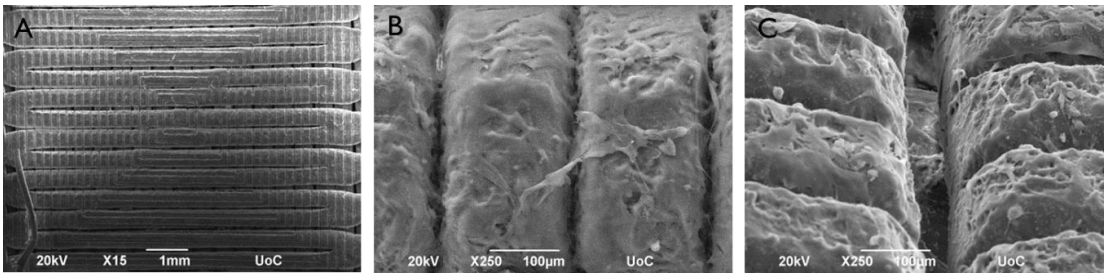

Figure 44: Top (A&B) and tilted (C) @ 45 º view of mesh with 100 μm space with ablated concentric squares 5ns, 5 KHz and 3.79 Watts and for 2 days in 100k MSCs culture.

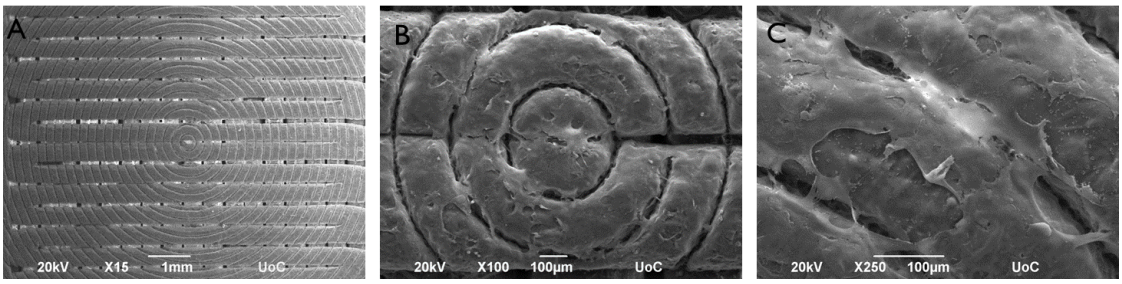

Figure 45: Top (A&B) and tilted (C) @ 45 º view of mesh with 100µm space with ablated concentric circles 5ns, 5 KHz and 3.79 Watts and for 2 days in 100k MSCs culture.

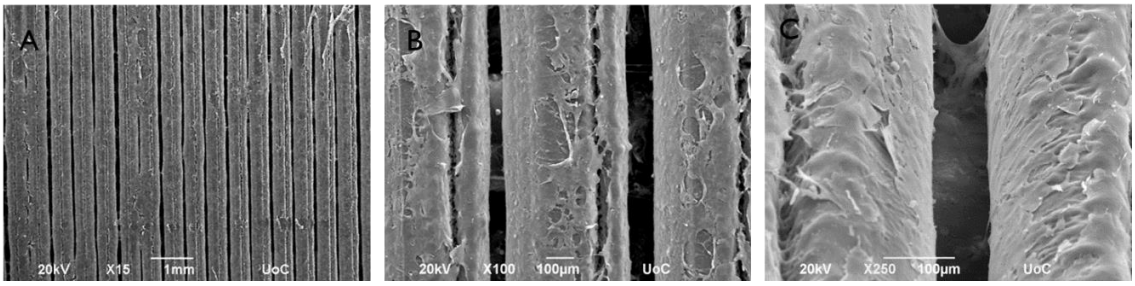

Figure 46: Top (A&B) and tilted (C) @ 45 º view of mesh with 100µm space and ablated grooves 5ns, 5 KHz and 3.79 Watts and with 2 days in 100k MSCs culture.

Figure 47 shows a flat natural PLA square with dimensions of 8x8x0.6 mm where we studied their interactions with MSCs of different concentrations and for different days of culture. We can observe that the cells proliferated and attached well on the surface for all the days and concentrations. We observed that the concentration of 50K MSCs was adequate and efficient for all the different cellular functions we were planning to investigate.

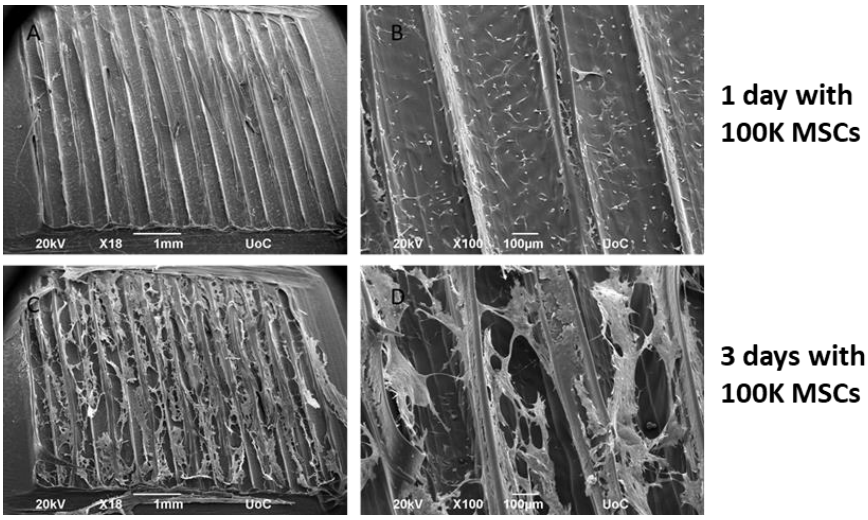

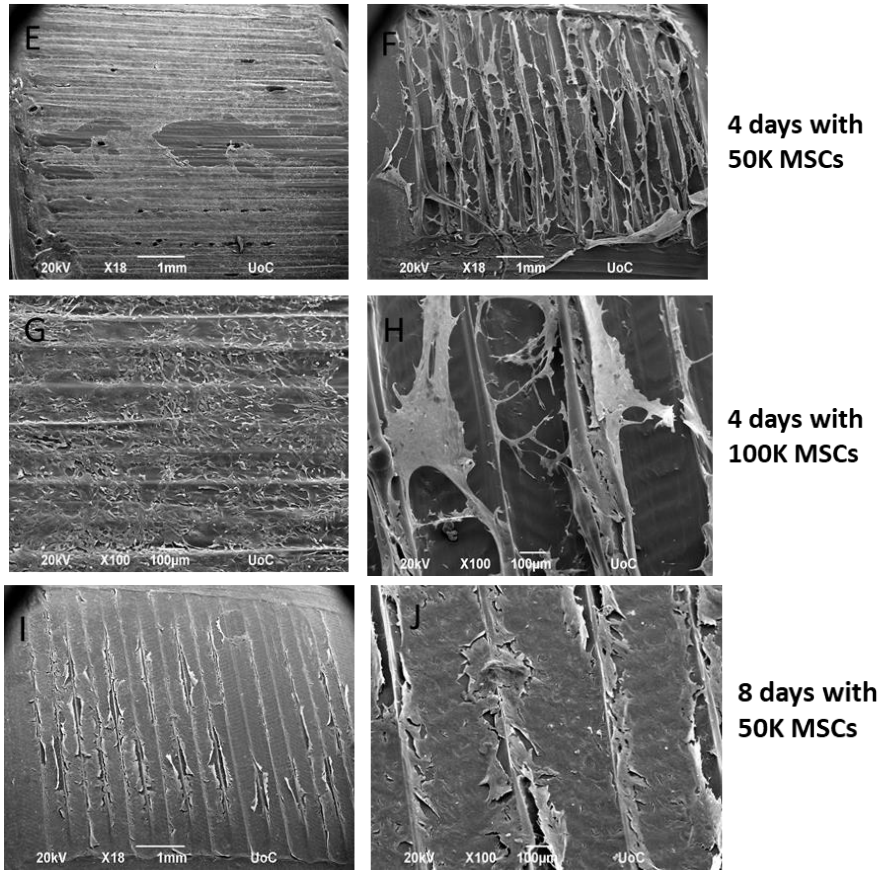

Figure 47: Tilted images @ 45 º of SEM for different days and MSCs' concentrations for the flat square 8x8x0.6 mm. (A) and (B) PLA flat for 1 day with 100K MSCs, (C) and (D) PLA flat for 3 days with 100K MSCs, (E) and (F) PLA flat for 4 days with 50K MSCs, (G) and (H) PLA flat for 4 days with 100K MSCs and (I) and (J) PLA flat for 3 days with 50K MSCs.

In Figure 48 is presented a mesh with dimensions 10x10 x1.80 with 9 ablated holes of diameter 0.07 mm with MSCs at different days of culture and concentrations. Unfortunately, the first four images are upside down so, we could not observe the behavior of cells inside the holes. The bigger holes that are presented in these images are mistake of the printer's design. We can observe that again the cells proliferated and attached well at the bottom side of the scaffold. The MSCs proliferated inside the ablated holes and on top of them, between the lines of the mesh and after 3 days and at the layer underneath. At figure 48, we can see a detachment of the cells layer due to the sample SEM preparation and fixation protocol. Unfortunately, due to the wrong placement of the first scaffolds, we can make a clear comparison for 2 and 4 days. Although, it is clear that the cells proliferated more for the 4 days of culture.

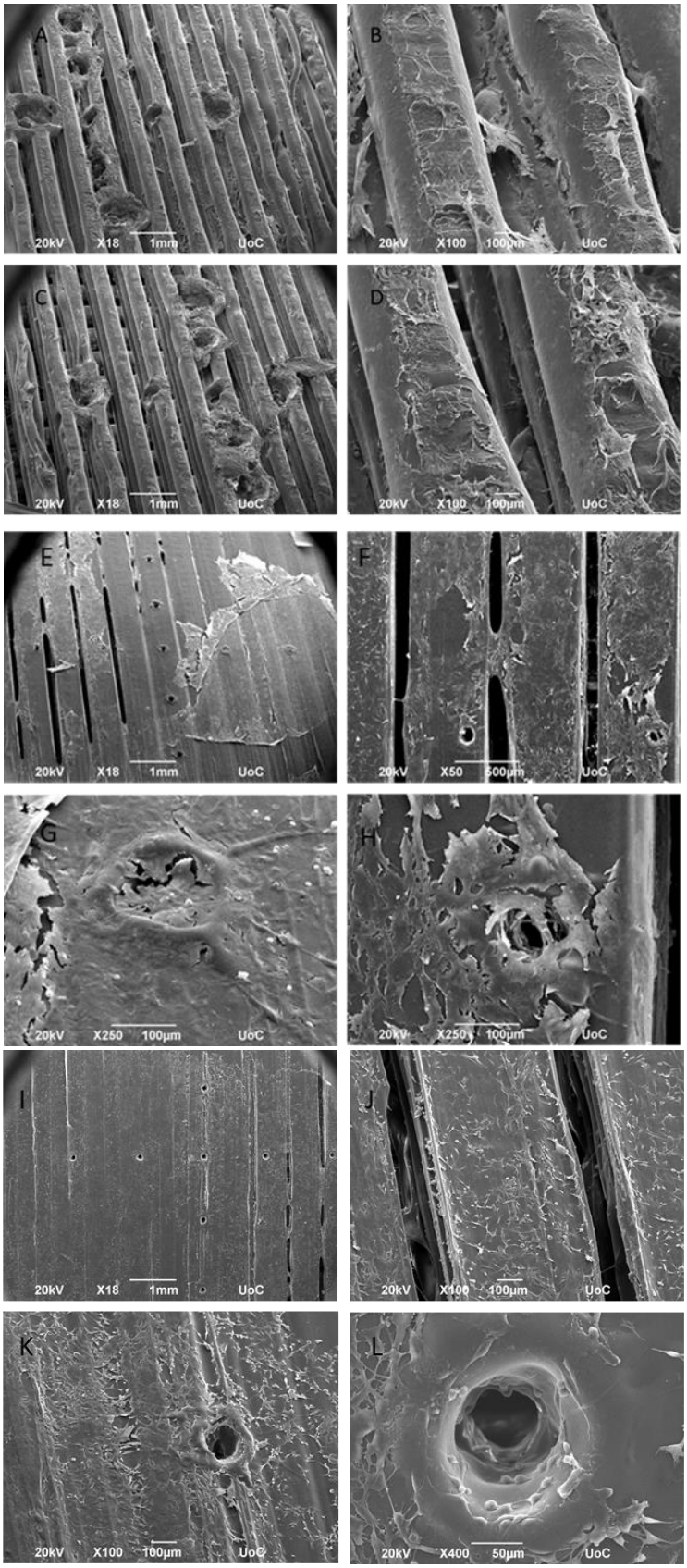

2 days of 100K MSCs culture.

3 days of 100K MSCs culture.

4 days of 50K MSCs culture.

4 days of 50K MSCs culture.

Figure 48: Top view and tilted images @ 45 ^{o} of SEM for meshes 10x10x1.80 with 9 laser ablated holes with 5ns, 2KHz and 1.91 Watts and diameter of 0.7 mm with two different MSCs concentrations for different days of culture. (A) and (B) 4D PLA with 9 holes for 2 day with 100K MSCs, (C) and (D) 4D PLA with 9 holes for 3 days with 100K MSCs, (E),(F),(G) and (H) 4D PLA with 9 holes for 4 days with 50K MSCs and (I),(J), (K) and (L4D PLA with 9 holes for 4 days with 50K MSCs.

Figure 49 shows the results with MSCs for two different concentrations with a 4D mesh scaffold which has two different gaps (0.32 and 0.50 mm) between the straps. Figure 49 (A) and (B) refer to a 4D mesh that was places upside down. The rest of the 4D meshes demonstrated that the MSCs proliferated and attached well on the surface, inside and at the top of the holes. At 4 days and 7 days, the MSCs grew between the straps of the mesh and at the underneath layer. Finally, in figure 49 (G) and (H) for the 7 days, we can observe a cell detachment due to the various washes at the different stages of the SEM preparation and fixation protocol.

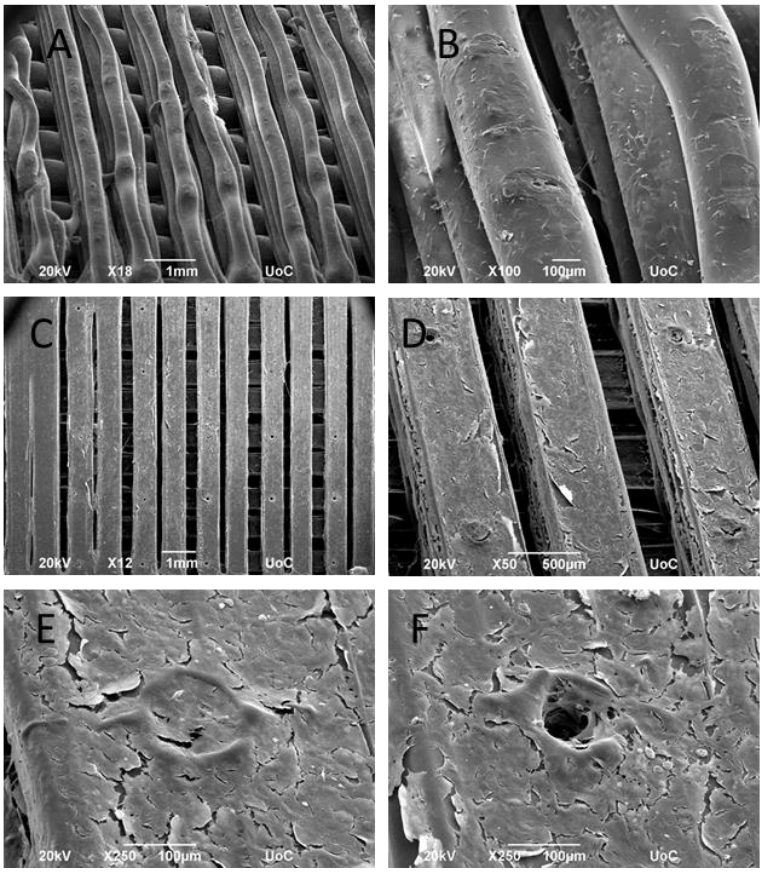

1 day of 100K MSCs culture

4 days of 50K MSCs culture

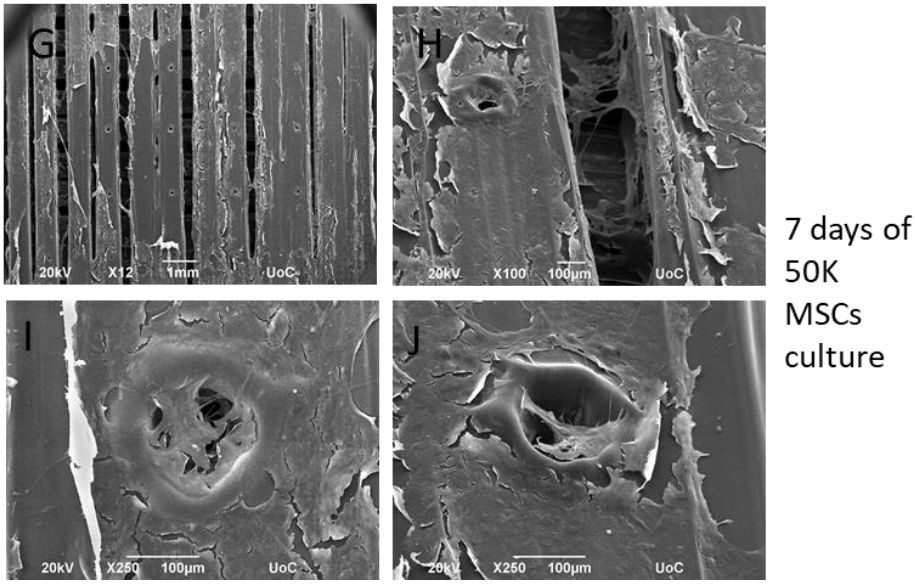

Figure 49: Top view and tilted images @ 45 º of SEM for meshes 10x10x1.80 with 30 laser ablated holes with 5ns, 2KHz and 1.91 Watts and diameter of 0.7 mm with two different concertation of MSCs for different days of culture.(A) and (B) 4D PLA with 30 holes for 1 day with 100K MSCs, (C), (D),(E) and (F) 4D PLA with 30 holes for 4 days with 100K MSCs, (G), (H),(I) and (J) 4D PLA with 30 holes for 7 days with 50K MSCs

Figure 50,51 and 52 depict the orthogonal scaffold with 3 different depths of ablated microcavities (0.15, 0.45 and 0.90 mm) with dimensions of 0.5x1 mm. In this case, we wished to investigate what is the effect of the scaffold's microcavities on the MSCs' attachment and proliferation. We can see from the first days of culture that the microcavities' depth indeed plays a role for the specific cellular responses. The 0.15 mm microcavity depth appears to have more MSCs in comparison with the other microcavities . MSCs adhered on the walls and on the bottom of all the microcavities, however on 0.15mm depth appeared to have covered completely the whole bottom area and all the walls in comparison with the other wells.

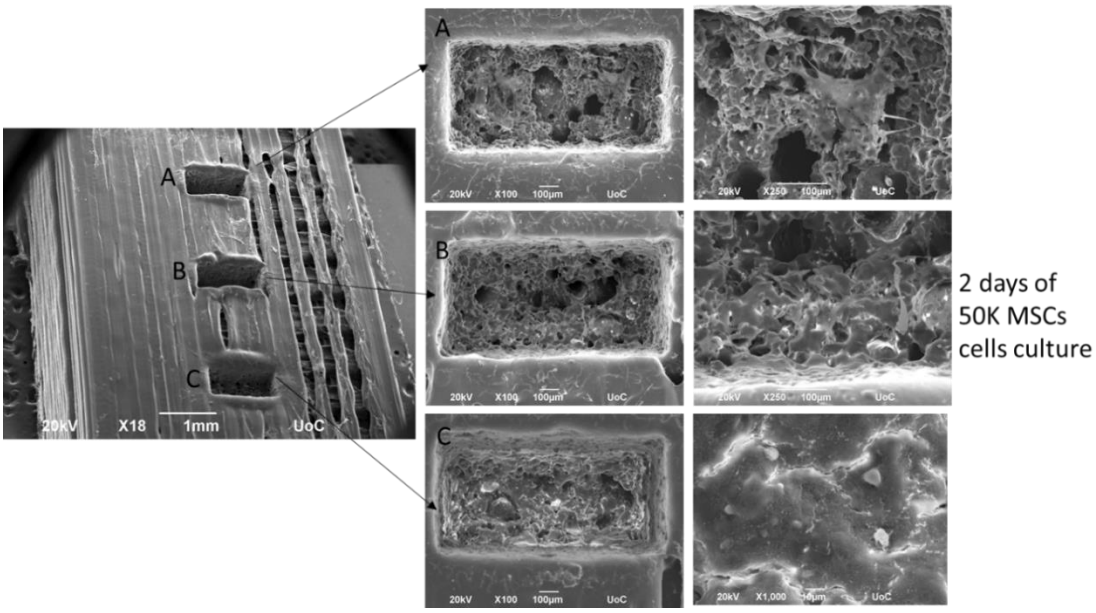

Figure 50: Top and tilted view @ 45 º of SEM images for orthogonal with 3 different depth of ablated microcavities (0.15 (A), 0.45(B) and 0.90 (C) mm) and distances 1x0.5 with laser parameters 5ns, 5KHz, 3,92 Watts, 100mm/sec and mark time =16 with 50K concertation of MSCs cells for 2 days of culture.

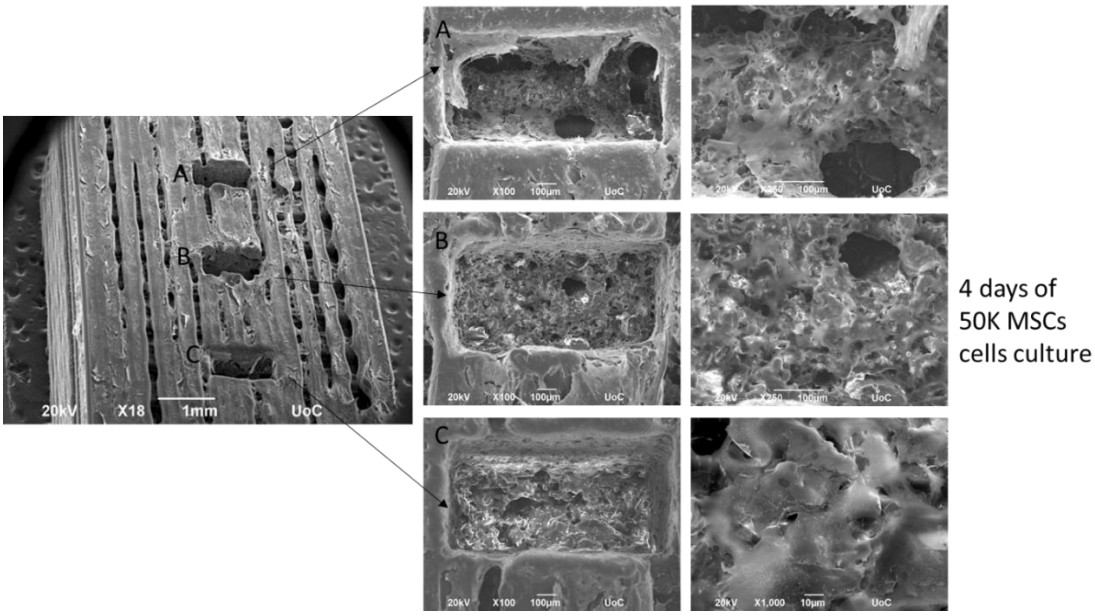

Figure 51: Top and tilted view@ 45 º of SEM images for orthogonal with 3 different depth of ablated microcavities (0.15 (A), 0.45(B) and 0.90 (C) mm) and distances 1x0.5 with laser parameters 5ns, 5KHz, 3,92 Watts, 100mm/sec and mark time =16 with 50K concertation of MSCs cells for 4 days of culture.

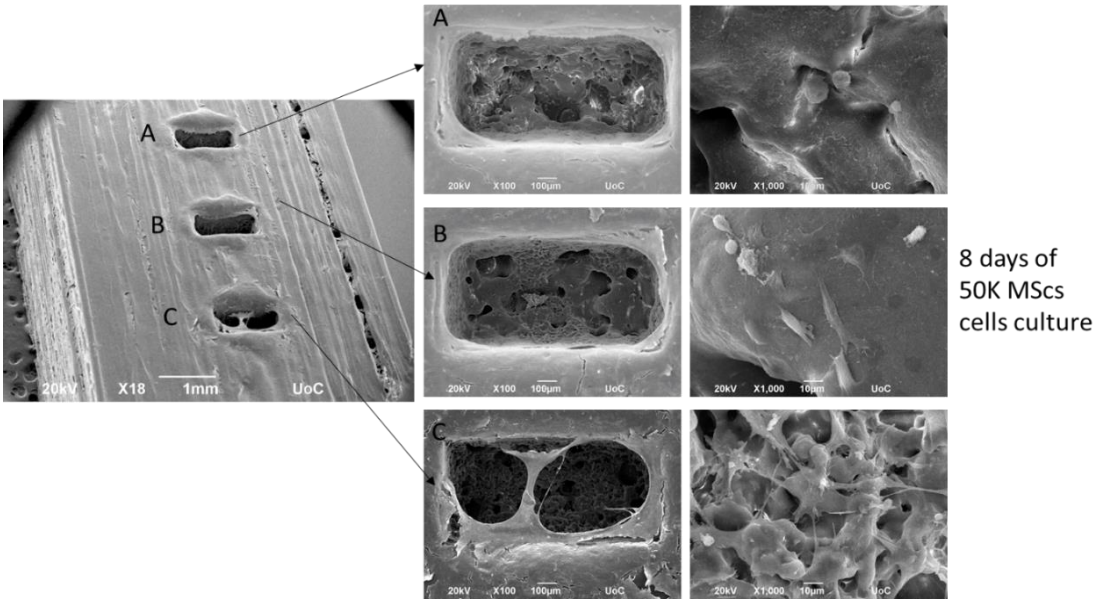

Figure 52: Top and tilted view @ 45 º of SEM images for orthogonal with 3 different depth of ablated microcavities (0.15 (C), 0.45(B) and 0.90 (A) mm) and distances 1x0.5 with laser parameters 5ns, 5KHz, 3,92 Watts, 100mm/sec and mark time =16 with 50K concertation of MSCs cells for 8 days of culture.

Figure 53,54 and 55 present the orthogonal scaffold with 3 different depths of ablated microcavities (0.15, 0.45 and 0.90 mm) and dimensions of 1x2 mm. In these scaffolds, we attempted to place/seed the cells only inside of the ablated microcavities in order to study the effect of microcavity depth on the adhesion, proliferation and migration

of cells. We can see from the first days of culture that the microcavity depth indeed plays a significant role on cellular responses. The 0.15 mm microcavity depth seems that has a greater cell number than the other wells. Such a finding could be ideal for fabricating scaffolds with different structures (microcavity height, size) that will allow cells to grow and proliferate at different times at sites with specific tissue function e.g. bone.

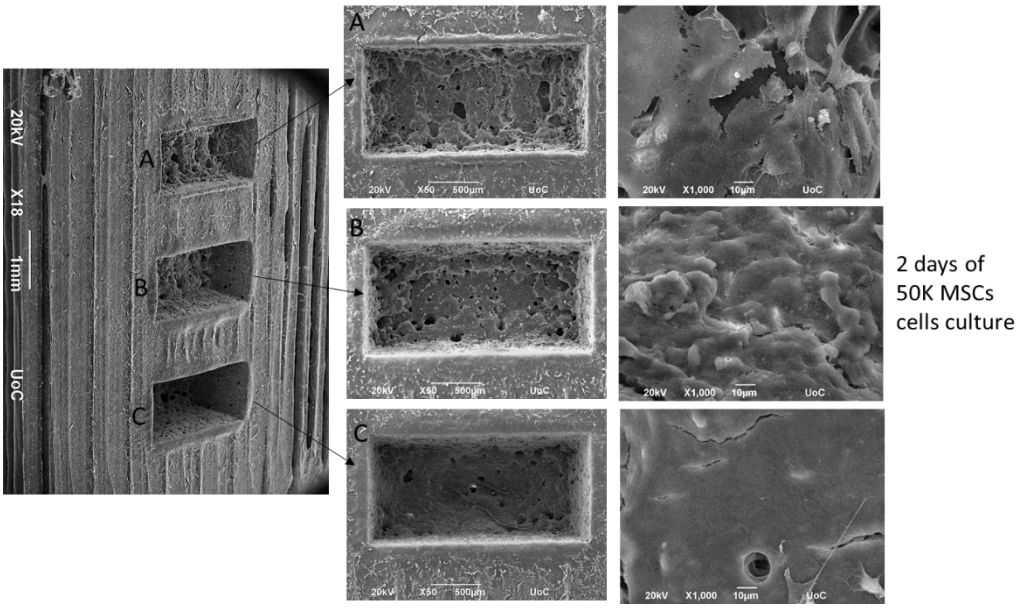

Figure 53: Top and tilted view @ 45 º of SEM images for orthogonal with 3 different depth of ablated rectangles (0.15(A), 0.45(B) and 0.90(C)mm) and distances 2x1 with laser parameters 5ns, 5KHz, 3,92 Watts, 100mm/sec and mark time =16 with 50K concertation of MSCs cells for 2 days of culture.

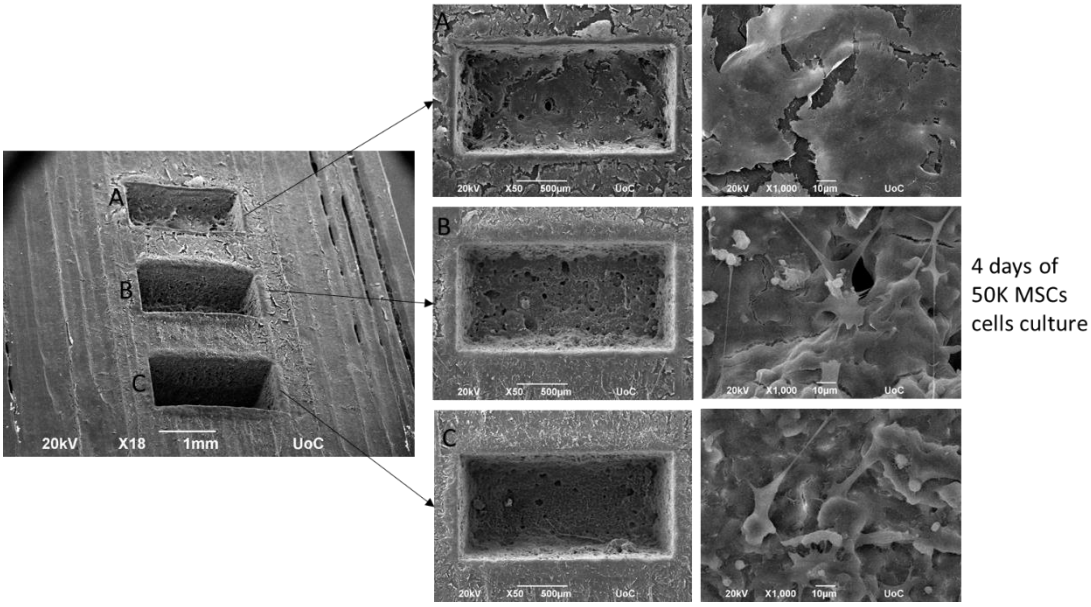

Figure 54: Top and tilted view @ 45 º of SEM images for orthogonal with 3 different depth of ablated rectangles (0.15(A), 0.45(B) and 0.90(C)mm) and distances 2x1 with laser parameters 5ns, 5KHz, 3,92 Watts, 100mm/sec and mark time =16 with 50K concertation of MSCs cells for 4 days of culture.

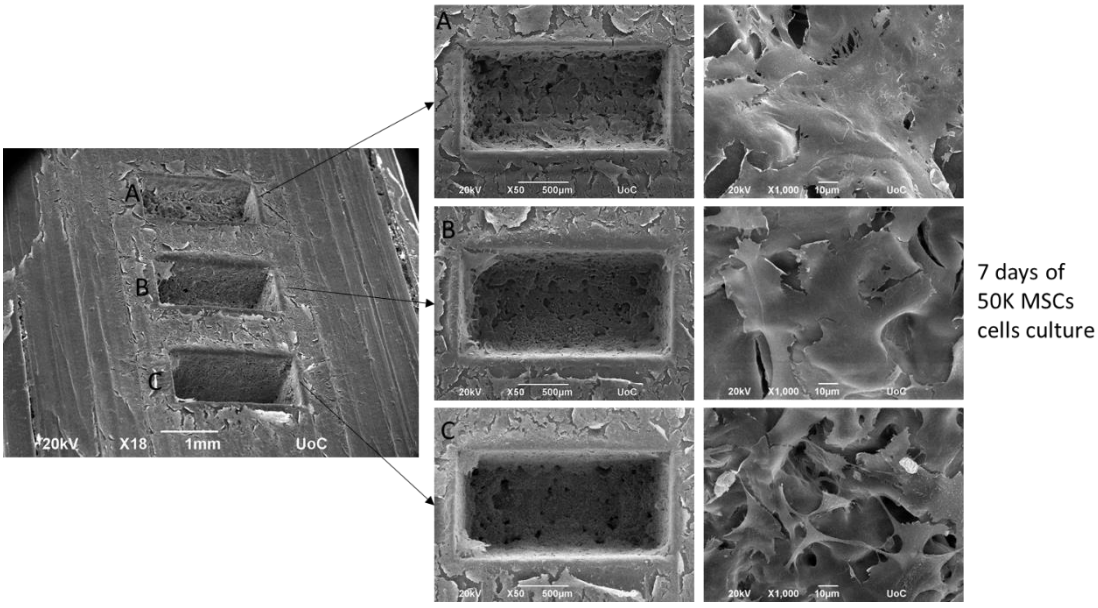

Figure 55: Top and tilted view @ 45 º of SEM images for orthogonal with 3 different depth of ablated rectangles (0.15(A), 0.45(B) and 0.90(C)mm) and distances 2x1 with laser parameters 5ns, 5KHz, 3,92 Watts, 100mm/sec and mark time =16 with 50K concertation of MSCs cells for 7 days of culture.

1.4.2 Results of Confocal Microscope

Figure 56 depicts representative images of cell morphology, proliferation and mechanotransduction obtained by confocal microscope on tissue culture plastics (TCP) as control and on 4D PLA meshes. Immunofluorescent staining was used to examine cell cytoskeleton (actin Phalloidin) at 568 nm, cell mechanotransduction (YAP/TAZ) at 647 nm and cell nucleus (DAPI) with a UV lamp on these surfaces. We

can observe that the cells adhered on the surfaces and they grew also in the holes. In addition, we can see nuclear YAP localization at the 4D PLA meshes indicating the PLA stiffness but at the same time, the ability of MSCs to differentiate to osteogenic lineage.

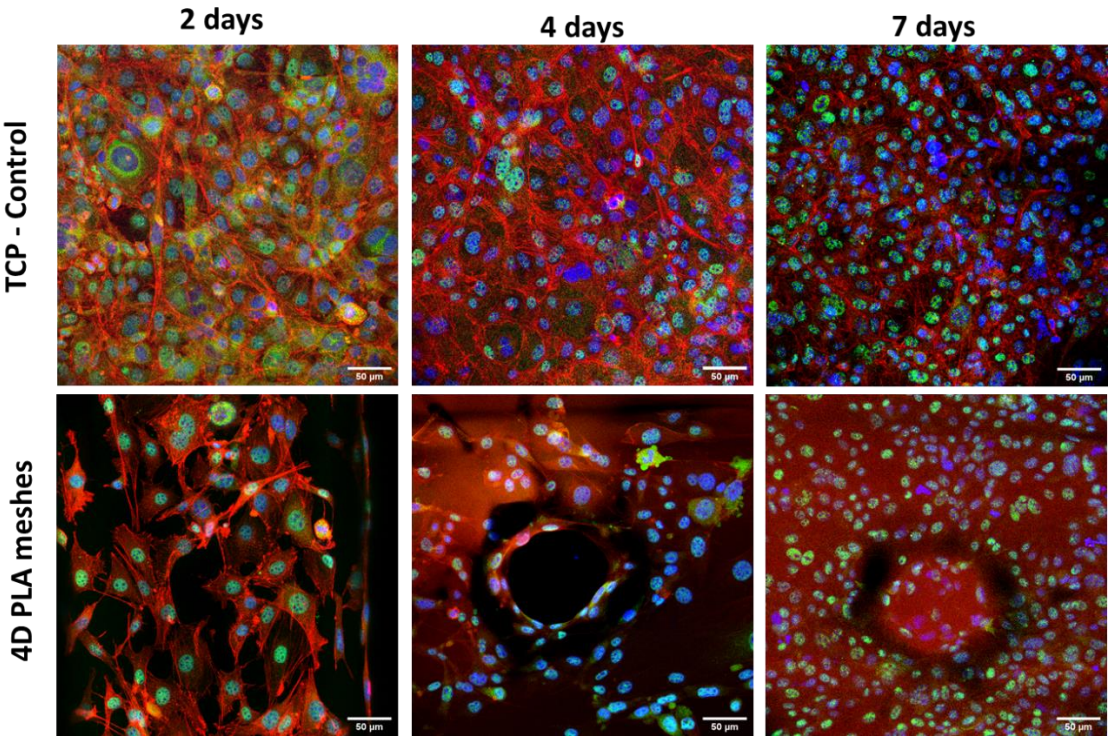

Figure 56: Confocal images of 4D PLA mesh and TCP (Control) with MSCs for 2d, 4d and 7d. **In blue colour** is the DAPI, representing the MSCs nucleus, in **green colour** is YAP showing the mechanosensing points, **in red colour** is Actin/Phalloidin representing the cytoskeleton.

Figure 57 shows representative images of cell morphology, proliferation and differentiation obtained by confocal microscope on tissue culture plastics (TCP) as control and on 4D PLA meshes. Immunofluorescent staining was used to examine Osteogenic lineage differentiation (Osteopontin(OPN)) at 647 nm and cell nucleus (DAPI) with UV lamp on these surfaces. We can observe that the immunofluorescence staining revealed that there is expression of osteogenic specific marker osteopontin in all groups. More specifically, for 3+6 days with osteo medium, there is a high OPN expression on MSCs in the 4D PLA mesh. For 2+11 days of culture with osteogenic medium, the OPN is clearly appeared in TCP control. In addition, for 3+14 days of culture with osteogenic medium, there is high OPN expression on both 4D PLA and in TCP control. At last, for 3+17 days of culture with osteogenic medium, there is high OPN expression on MSCs in the 4D PLA mesh. In general, for all the days of culture with osteo medium, there is a high OPN expression on MSCs in 4D PLA mesh and TCP control.

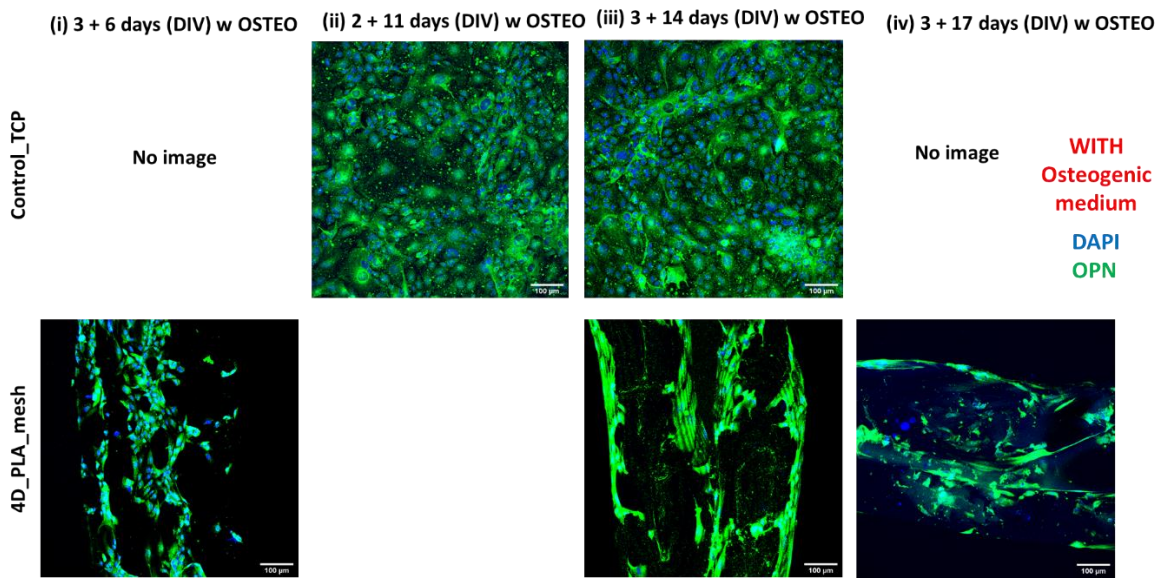

Figure 57: Confocal images of (i) 3 + 6 days (with osteogenic medium); (ii) 2 + 11 days (with osteogenic medium); (iii) 3 + 14 days (with osteogenic medium) and (iv) 3 + 17 days (with osteogenic medium) of TCP control and 4D printed PLA in direct contact with MSCs (cell no 50k/ml). The 'no image' indication means that there were no control samples for these time points.

Figure 58 depicts representative images of cell morphology, proliferation and differentiation obtained by confocal microscope on tissue culture plastics (TCP) as control and on 4D PLA meshes. Immunofluorescent staining was used to examine cell Osteogenic lineage differentiation (Osteopontin(OPN)) at 647 nm and cell nucleus (DAPI) with UV lamp on these surfaces. We can observe that without osteogenic medium the immunofluorescence staining revealed that there is expression of osteogenic specific marker osteopontin in all groups. More specifically, for 13 days without osteogenic medium, there are signs of OPN expression on MSCs in the 4D PLA mesh, while there are low OPN expression at TCP. For 16 days of culture without osteogenic medium, the OPN is clearly appeared in TCP control. There is a higher OPN expression on 4D PLA mesh compared to TCP. At last, for 23 days of culture without osteogenic medium, there is high OPN expression on both 4D PLA and in TCP control. In general, for all the days of culture without osteogenic medium, there is OPN expression on MSCs in 4D PLA mesh and TCP control although, for 16 days the OPN expression is higher at 4D PLA meshes that TCP control.

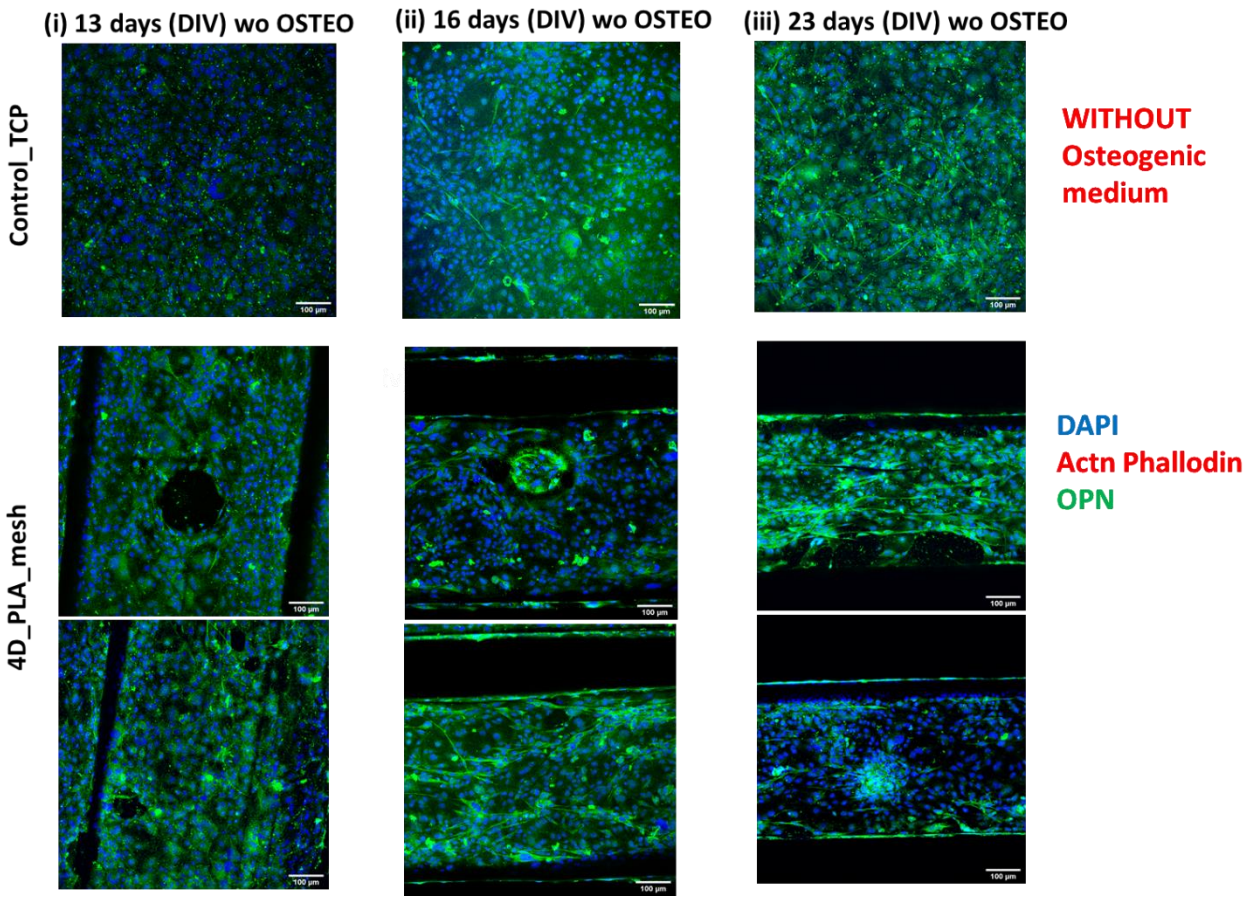

Figure 58: Confocal images of (i) 13 days (without osteogenic medium); (ii) 16 days (without osteogenic medium) and (iii) 23 days (without osteogenic medium) of TCP control and 4D printed PLA in direct contact with MSCs (cell no 50k/ml).

The figure 59 shows representative images of cell morphology, proliferation and differentiation obtained by confocal microscope on tissue culture plastics (TCP) as control and on PLA flat. Immunofluorescent staining was used to examine cell, Osteogenic lineage differentiation (Osteopontin(OPN)) at 647 nm and cell nucleus (DAPI) with UV lamp on these surfaces. We can observe that without osteogenic medium the immunofluorescence staining revealed that there is expression of osteogenic specific marker osteopontin in all groups. More specifically, for 23 days without osteogenic medium, there is a high expression of OPN on MSCs without the osteogenic factor; and in comparison, there is higher OPN expression on PLA flat compared with the TCP.

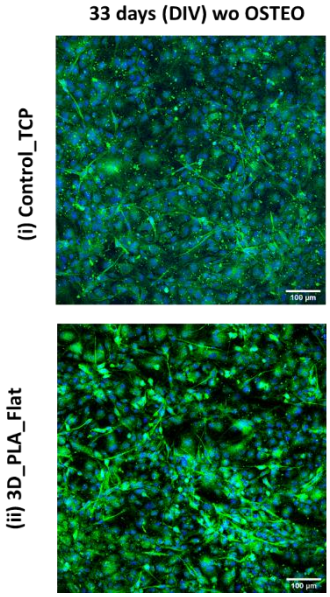

Figure 59: Confocal images of i) TCP control; and ii) 3D printed PLA flat in direct contact with MSCs for 23 days (without osteogenic medium) (cell no 50k/ml).

Conclusion

In this master defense, we successfully made the innovative combination of additive manufacturing and subtractive technique to fabricate 4D PLA scaffolds for tissue engineering. We succeeded it, after the change of two set-ups, many parametric experiments, changes in the construction of the 3D printer, construction of the optical path, alignments, a custom-made software, and many experiments. Eventually, we managed to make three different groups of 4D scaffolds for Tissue Engineering, with laser features that had resolution smaller than the resolution of the 3D printer.

We characterized the morphology, structure, optical properties, and wettability of the PLA samples via SEM, UV-Vis method and contact angle technique respectively. The SEM images showed that the surfaces were in general smooth, without gaps and that the holes had a diameter of 0.8 mm approximately. Moreover, we observed that with and without laser the PLA scaffolds were hydrophilic. At last, UV-Vis measurements showed that the transmittance of PLA samples with and without laser were the same.

Then we cultured MSCs on PLA flats and 4D PLA scaffolds. We observed their morphology with SEM where they attached and proliferated well at all the surfaces. Specifically, we observed an increase in cell number as we increased the days of culture (successful proliferation). MSCs also preferred the shallower microcavities of the PLA meshes. . Finally, we observed the cellular responses such as adhesion via cell cytoskeleton cell mechanotransduction via YAP and differentiation to osteogenic lineage via osteopontin . The conclusions were that there was an osteogenic lineage differentiation at culture MSCs cells with and without osteogenic medium. The PLA flat and 4D scaffolds are enough to induce osteogenesis, independently of culture

medium conditions. The above finding was complemented by the nucleus localization of YAP in MSCs when in contact with the PLA samples. Moreover, YAP localization on the MSC nucleus demonstrated the stiffness of PLA. Such 4D printed scaffolds with controlled micro and macro-porosities could be advanced and safer solutions for treating tissue defects e.g., bone without additional agents.

In the future, further experiments and corrections of the set-up are suggested. At first, the software of the set-up requires further corrections. Secondly, the stability of specific mirrors of the set-up is of great importance. Thirdly, in order to justify and enhance the osteogenic lineage of the MSCs in contact with the PLA scaffolds, further experiments are required such as ALP and alizarin red staining studies of 4D PLA meshes from 7 days with and without osteogenic differentiation medium. The concentration of osteogenic cell-differentiation markers is crucial for successful implantation. ALP is considered as an early marker, osteopontin as a middle marker, and as a late marker is the concentration of calcium revealed by Alizarin Red staining. In addition, we must repeat the experiment with osteogenic medium in order to be sure for our results. Finally, the use of a softer material e.g. cellulose and/or PHB will be ideal to demonstrate further the possibilities and enhance the proof-of-concept of this advanced 4D printing system.

Bibliography

1. Harris, M., Potgieter, J., Archer, R. & Arif, K. M. Effect of material and process specific factors on the strength of printed parts in fused filament fabrication: A review of recent developments. *Materials (Basel).* **12**, (2019).

2. Ye, G., Wang, W., Fan, D. & He, P. Effects of femtosecond laser micromachining on the surface and substrate properties of poly-lactic acid (PLA). *Appl. Surf. Sci.* **538**, 148117 (2021).

3. Han, X. *et al.* An In Vitro Study of Osteoblast Response on Fused-Filament Fabrication 3D Printed PEEK for Dental and Cranio-Maxillofacial Implants. *J. Clin. Med.* **8**, 771 (2019).

4. Lasprilla, A. J. R., Martinez, G. A. R., Lunelli, B. H., Jardini, A. L. & Filho, R. M. Poly-lactic acid synthesis for application in biomedical devices - A review. *Biotechnol. Adv.* **30**, 321–328 (2012).

5. Daminabo, S. C., Goel, S., Grammatikos, S. A., Nezhad, H. Y. & Thakur, V. K. Fused deposition modeling-based additive manufacturing (3D printing): techniques for polymer material systems. *Mater. Today Chem.* **16**, 100248 (2020).

6. Stansbury, J. W. & Idacavage, M. J. 3D printing with polymers : Challenges among expanding options and opportunities. *Dent. Mater.* **32**, 54–64 (2015).

7. Tamay, D. G., Usal, T. D., Alagoz, A. S. & Yucel, D. 3D and 4D Printing of Polymers for Tissue Engineering Applications. **7**, (2019).

8. Szymczyk-ziólkowska, P., Beata, M., Detyna, J., Michalak, I. & Gruber, P. ScienceDirect A review of fabrication polymer scaffolds for biomedical applications using additive manufacturing techniques. **0**, (2020).

9. Zhang, L., Yang, G., Johnson, B. N. & Jia, X. Acta Biomaterialia Three-dimensional (3D) printed scaffold and material selection for bone repair. *Acta Biomater.* **84**, 16–33 (2019).

10. Objects, A. *TAZ 5 User Manual*.

11. Ortiz, R. *et al.* Laser surface microstructuring of a bio-resorbable polymer to anchor stem cells, control adipocyte morphology, and promote osteogenesis. *Polymers (Basel).* **10**, (2018).

12. Malinauskas, M. *et al.* 3D microporous scaffolds manufactured via combination of fused filament fabrication and direct laser writing ablation. *Micromachines* **5**, 839–858 (2014).

13. Ravi-Kumar, S., Lies, B., Lyu, H. & Qin, H. Laser ablation of polymers: A review. **34**, 316–327 (2019).

14. Mittal, K. L. Part 2 OTHER EFFECTS / APPLICATIONS OF LASER SURFACE TREATMENT Fundamentals of Laser-Polymer Interactions and their Relevance to Polymer Metallization. (2015).

15. Tran, D. V. *et al.* Femtosecond laser processing of crystalline silicon. (2005).

16. Bonse, J., Wrobel, J. M., Krüger, J. & Kautek, W. Ultrashort-pulse laser ablation of indium phosphide in air. *Appl. Phys. A Mater. Sci. Process.* **72**, 89–94 (2001).

17. Uğuz, H. *et al.* ce pte d M us pt. *J. Phys. Energy* **2**, 0–31 (2020).

18. Babaliari, E. *et al.* Engineering cell adhesion and orientation via ultrafast laser fabricated microstructured substrates. *Int. J. Mol. Sci.* **19**, (2018).

19. Zonderland, J. & Moroni, L. Steering cell behavior through mechanobiology in 3D: A regenerative medicine perspective. *Biomaterials* **268**, 120572 (2021).

20. Ntege, E. H., Sunami, H. & Shimizu, Y. Advances in regenerative therapy: A review of the literature and future directions. *Regen. Ther.* **14**, 136–153 (2020).

21. Qu, H., Fu, H., Han, Z. & Sun, Y. Biomaterials for bone tissue engineering scaffolds: A review. *RSC Adv.* **9**, 26252–26262 (2019).

22. Canette, A. & Briandet, R. *Microscopy: Confocal Laser Scanning Microscopy*. *Encyclopedia of Food Microbiology: Second Edition* vol. 2 (Elsevier, 2014).

23. Ye, G., Wang, W., Fan, D. & He, P. Effects of femtosecond laser micromachining on the surface and substrate properties of poly-lactic acid (PLA). *Appl. Surf. Sci.* **538**, (2021).

24. Shibuya, T. *et al.* Ablation thresholds and morphological changes of poly-l-lactic acid for pulse durations in the femtosecond-to-picosecond regime. *Surf. Interface Anal.* **52**, 1145–1149 (2020).

25. https://www.makeitfrom.com/material-properties/Polylactic-Acid-PLA-Polylactide

26. https://formlabs.com/blog/additive-manufacturing-vs-subtractive-manufacturing/

27. https://www.goodwin.edu/enews/what-is-cnc/

28. https://en.wikipedia.org/wiki/Electrical_discharge_machining

29. https://en.wikipedia.org/wiki/Laser_cutting

30. https://en.wikipedia.org/wiki/Water_jet_cutter

31. https://www.orc.soton.ac.uk/how-fibre-lasers-work

32. https://www.laserlabsource.com/Solid-State-Lasers/fiber-laser-basics-and-design-principle.

33. Laser Damaged Threshold, Edmund optics

34. https://www.nanoscience.com/techniques/scanning-electron-microscopy/

35. https://www.thermofisher.com/blog/microscopy/what-is-sem-scanning-electron-microscopy-explained/

36. https://www.ssi.shimadzu.com/products/uv-vis-spectrophotometers/faqs/solid-sample-transmission.html

37. https://resources.perkinelmer.com/lab-solutions/resources/docs/APP_UseofUVVisNIRinDevelopmentPV.pdf

38. https://www.agilent.com/cs/library/primers/public/primer-uv-vis-basics-5980-1397en-agilent.pdf

39. https://en.wikipedia.org/wiki/Wetting

40. S. Khetan, M. Guvendiren, W.R. Legant, D.M. Cohen, C.S. Chen, J.A. Burdick, Degradation-mediated cellular traction directs stem cell fate in covalently crosslinked three-dimensional hydrogels, Nat. Mater. **12** (5) (2013) 458–465.

41. S.A. Ferreira, M.S. Motwani, P.A. Faull, A.J. Seymour, T.T.L. Yu, M. Enayati, D. K. Taheem, C. Salzlechner, T. Haghighi, E.M. Kania, O.P. Oommen, T. Ahmed, S. Loaiza, K. Parzych, F. Dazzi, O.P. Varghese, F. Festy, A.E. Grigoriadis, H. W. Auner, A.P. Snijders, L. Bozec, E. Gentleman, Bi-directional cell-pericellular matrix interactions direct stem cell fate, Nat. Commun. **9** (1) (2018) 4049.

42. Y. Tang, R.G. Rowe, E.L. Botvinick, A. Kurup, A.J. Putnam, M. Seiki, V. M. Weaver, E.T. Keller, S. Goldstein, J. Dai, D. Begun, T. Saunders, S.J. Weiss, MT1-MMP-dependent control of skeletal stem cell commitment via a beta1- integrin/YAP/TAZ signaling axis, Dev. Cell **2**5 (4) (2013) 402–416.

43. H.J. Kong, D. Kaigler, K. Kim, D.J. Mooney, Controlling rigidity and degradation of alginate hydrogels via molecular weight distribution, Biomacromolecules **5** (5) (2004) 1720–1727.

44. S.I. Fraley, Y. Feng, R. Krishnamurthy, D.H. Kim, A. Celedon, G.D. Longmore, D. Wirtz, A distinctive role for focal adhesion proteins in three-dimensional cell motility, Nat. Cell Biol**. 12** (6) (2010) 598–604.

45. Byron D. Gates, Nanofabrication with molds & stamps, *Materials Today*, Volume **8**, Issue 2, 2005, Pages 44-49, ISSN 1369-7021.

46. Birmingham, E., Niebur, G. L., & McHugh, P. E. (2012). Osteogenic differentiation of mesenchymal stem cells is regulated by osteocyte and osteoblast cells in a simplified bone niche. *European Cells and Materials*, ***23***, 13-27.

47. Rutkovskiy, A., Stensløkken, K. O., & Vaage, I. J. (2016). Osteoblast differentiation at a glance. *Medical science monitor basic research*, ***22***, 95.

48. Sell, S. (Ed.). (2013). *Stem cells handbook*. Springer Science & Business Media.

49. Moosazadeh Moghaddam, M., Bonakdar, S., Shokrgozar, M. A., Zaminy, A., Vali, H., & Faghihi, S. (2019). Engineered substrates with imprinted cell-like topographies induce direct differentiation of adipose-derived mesenchymal stem cells into Schwann cells. *Artificial cells, nanomedicine, and biotechnology*, ***47***(1), 1022-1035.

50. Ma, S., Xie, N., Li, W., Yuan, B., Shi, Y., & Wang, Y. (2014). Immunobiology of mesenchymal stem cells. *Cell Death & Differentiation*, ***21***(2), 216-225.

60. Alksne, M. *et al.* The effect of larger than cell diameter polylactic acid surface patterns on osteogenic differentiation of rat dental pulp stem cells. *J. Biomed. Mater. Res. - Part A* **107**, 174–186 (2019).